Since January 2020 Elsevier has created a COVID-19 resource centre with free information in English and Mandarin on the novel coronavirus COVID-19. The COVID-19 resource centre is hosted on Elsevier Connect, the company's public news and information website.

Cell

Germinal center responses to SARS-CoV-2 mRNA vaccines in healthy and immunocompromised individuals

Graphical abstract

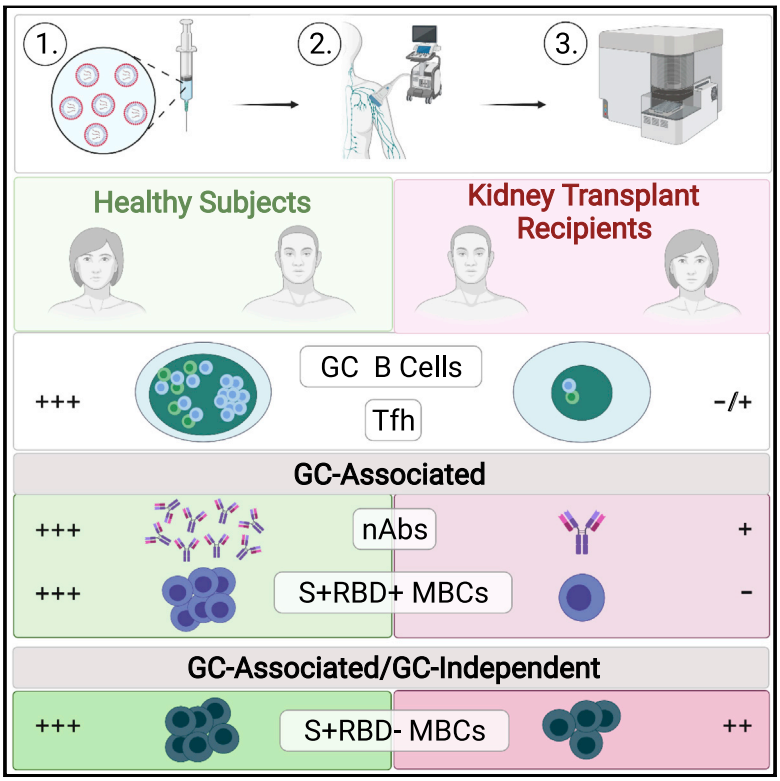

Highlights

- Human GC responses to SARS-CoV-2 vaccines are restricted to draining lymph nodes
- Vaccine-induced GC responses are associated with SARS-CoV-2 neutralizing antibodies
- Kidney transplant recipients lack GC responses to SARS-CoV-2 vaccines
- Vaccines expand S+RBD− memory B cells in healthy donors and transplant recipients

Authors

Katlyn Lederer, Emily Bettini, Kalpana Parvathaneni, ..., Ali Naji, Vijay Bhoj, Michela Locci

Correspondence

ali.naji@pennmedicine.upenn.edu (A.N.), vbhoj@pennmedicine.upenn.edu (V.B.), michela.locci@pennmedicine.upenn.edu (M.L.)

In brief

Fine-needle aspiration of lymph nodes in humans reveals that SARS-CoV-2 vaccination induces neutralizing antibody-producing germinal centers, enhanced by repeated vaccination. Conversely, in patients receiving immunosuppressant medication, this process is disrupted, resulting in stunted protective immune responses, highlighting issues about vaccine and booster efficacy in patients with compromised immune systems.

Lederer et al., 2022, Cell *185*, 1008–1024
March 17, 2022
https://doi.org/10.1016/j.cell.2022.01.027

CellPress

CellPress

Cell

Article

Germinal center responses to SARS-CoV-2 mRNA vaccines in healthy and immunocompromised individuals

Katlyn Lederer,[1,2] Emily Bettini,[1,2] Kalpana Parvathaneni,[1,3,4] Mark M. Painter,[1,5] Divyansh Agarwal,[6] Kendall A. Lundgreen,[2] Madison Weirick,[1,2] Kavitha Muralidharan,[1,3,4] Diana Castaño,[7] Rishi R. Goel,[1,5] Xiaoming Xu,[1,4] Elizabeth M. Drapeau,[1,2] Sigrid Gouma,[1,2] Jordan T. Ort,[1,2] Moses Awofolaju,[1,2] Allison R. Greenplate,[1,5] Carole Le Coz,[1,8] Neil Romberg,[1,8] Jennifer Trofe-Clark,[9] Gregory Malat,[9] Lisa Jones,[10] Mark Rosen,[10] Daniela Weiskopf,[11] Alessandro Sette,[11,12] Behdad Besharatian,[13] Mary Kaminiski,[14] Scott E. Hensley,[1,2] Paul Bates,[2] E. John Wherry,[1,5] Ali Naji,[1,14,*] Vijay Bhoj,[1,3,4,*] and Michela Locci[1,2,15,*]

[1]Institute for Immunology, Perelman School of Medicine, University of Pennsylvania, Philadelphia, PA 19104, USA
[2]Department of Microbiology, Perelman School of Medicine, University of Pennsylvania, Philadelphia, PA 19104, USA
[3]Department of Pathology and Laboratory Medicine, Perelman School of Medicine, University of Pennsylvania, PA 19104, USA
[4]Center for Cellular Immunotherapies, Perelman School of Medicine, University of Pennsylvania, Philadelphia, PA 19104, USA
[5]Department of Systems Pharmacology and Translational Therapeutics, Perelman School of Medicine, University of Pennsylvania, PA 19104, USA
[6]Department of Surgery, Massachusetts General Hospital, Harvard Medical School, Boston, MA 02114, USA
[7]Grupo de Inmunología Celular e Inmunogenética, Facultad de Medicina, Universidad de Antioquia, Medellín, Antioquia 050010, Colombia
[8]Division of Immunology and Allergy, Children's Hospital of Philadelphia, Philadelphia, PA 19104, USA
[9]Department of Medicine, Renal Electrolyte and Hypertension Division, Perelman School of Medicine, University of Pennsylvania, Philadelphia, PA 19104, USA
[10]Department of Radiology, Division of Medicine, University of Pennsylvania, Philadelphia, PA 19104, USA
[11]Center for Infectious Disease and Vaccine Research, La Jolla Institute for Immunology, La Jolla, La Jolla, CA 92037, USA
[12]Department of Medicine, Division of Infectious Diseases and Global Public Health, University of California, San Diego (UCSD), La Jolla, La Jolla, CA 92093, USA
[13]Department of Medicine, Perelman School of Medicine, University of Pennsylvania, Philadelphia, PA 19104, USA
[14]Department of Surgery, Perelman School of Medicine at the University of Pennsylvania, Philadelphia, PA 19104, USA
[15]Lead contact
*Correspondence: ali.naji@pennmedicine.upenn.edu (A.N.), vbhoj@pennmedicine.upenn.edu (V.B.), michela.locci@pennmedicine.upenn.edu (M.L.)
https://doi.org/10.1016/j.cell.2022.01.027

SUMMARY

Vaccine-mediated immunity often relies on the generation of protective antibodies and memory B cells, which commonly stem from germinal center (GC) reactions. An in-depth comparison of the GC responses elicited by SARS-CoV-2 mRNA vaccines in healthy and immunocompromised individuals has not yet been performed due to the challenge of directly probing human lymph nodes. Herein, through a fine-needle aspiration-based approach, we profiled the immune responses to SARS-CoV-2 mRNA vaccines in lymph nodes of healthy individuals and kidney transplant recipients (KTXs). We found that, unlike healthy subjects, KTXs presented deeply blunted SARS-CoV-2-specific GC B cell responses coupled with severely hindered T follicular helper cell, SARS-CoV-2 receptor binding domain-specific memory B cell, and neutralizing antibody responses. KTXs also displayed reduced SARS-CoV-2-specific CD4 and CD8 T cell frequencies. Broadly, these data indicate impaired GC-derived immunity in immunocompromised individuals and suggest a GC origin for certain humoral and memory B cell responses following mRNA vaccination.

INTRODUCTION

Messenger RNA (mRNA) vaccines induce long-lasting, protective immune responses in animal models (Awasthi et al., 2019; Espeseth et al., 2020; Freyn et al., 2020; Pardi et al., 2017, 2018b, 2018a; Richner et al., 2017). This vaccine platform was first licensed for human use during the pandemic caused by severe acute respiratory syndrome coronavirus 2 (SARS-CoV-2) (Bettini and Locci, 2021; Carvalho et al., 2021; Krammer, 2020), and much still needs to be learned about the quality of the immune responses elicited by mRNA vaccines.

Most vaccines confer protection by eliciting antigen-specific antibodies (Abs) and memory B cells (MBCs) (Plotkin, 2010; Sallusto et al., 2010). Abs are secreted by plasma cells and can

potentially neutralize pathogens and prevent infections. Equally important are MBCs that act as a second line of defense and give rise to a quick burst of Ab-secreting plasma cells if the pathogens break through the "protective wall" of the pre-existing Abs. Plasma cells and MBCs are commonly generated during germinal center (GC) reactions (Allen et al., 2007; Mesin et al., 2016) in vaccine-draining lymph nodes (LNs). In GCs, activated B cells first undergo somatic hypermutation (SHM) in their immunoglobulin genes. Next, the high-affinity GC B cell clones resulting from the SHM process are positively selected and ultimately differentiate into long-lived plasma cells and MBCs. GC reactions are orchestrated by T follicular helper (Tfh) cells, specialized CD4 T cells that deliver a variety of signals shaping the fate of GC B cells (Crotty, 2019; Vinuesa et al., 2016). We and others have previously demonstrated that in mice, mRNA vaccines elicit potent GC responses closely intertwined with an efficient induction of SARS-CoV-2-specific neutralizing (nAbs) and MBCs (Lederer et al., 2020; Tai et al., 2020; Vogel et al., 2021), suggesting that GC reactions might be crucial to generate durable nAb and MBCs following SARS-CoV-2 vaccination. In line with these data, studies characterizing the immune responses to the SARS-CoV-2 mRNA vaccines in humans found a robust generation of nAbs and MBCs (Bettini and Locci, 2021; Collier et al., 2021; Edara et al., 2021; Goel et al., 2021; Jackson et al., 2020; Planas et al., 2021; Sahin et al., 2020; Stamatatos et al., 2021; Walsh et al., 2020; Wang et al., 2021a; Widge et al., 2021). However, with only one exception (Turner et al., 2021), all published human vaccine studies focused on the analysis of the immune responses measurable in peripheral blood. Hence, a thorough evaluation of the GC reactions driven by SARS-CoV-2 mRNA vaccines in humans, including their connection with nAbs and MBCs, is still missing.

Another question that warrants further investigation is whether SARS-CoV-2 mRNA vaccines can promote high-quality immune responses in individuals lacking a fully functional immune system, such as solid organ transplant recipients (SOTs). Immunosuppressant (IS) drugs administered to SOTs can cause a global immune system dysfunction spanning from defective antigen-presenting cell differentiation, maturation, and migration (Chen et al., 2004; Mehling et al., 2000; Piemonti et al., 1999) to direct suppression of T cells (Otsuka et al., 2021; Quéméneur et al., 2002; Taves and Ashwell, 2021; Vaeth et al., 2017) and, combined with anti-thymocyte globulin (ATG)-driven T cell depletion, can broadly hinder T cell responses including T cell help to B cells. Furthermore, IS drugs might directly affect the magnitude and quality of B cell responses (Eickenberg et al., 2012; Karnell et al., 2011). Analyses of blood samples from SOTs after SARS-CoV-2 vaccination has yielded mixed results (Benotmane et al., 2021; Boyarsky et al., 2021a, 2021b; Cucchiari et al., 2021; Kamar et al., 2021; Massa et al., 2021; Rincon-Arevalo et al., 2021). Some studies suggested that a fraction of SOTs can generate detectable SARS-CoV-2-binding Ab titers, whereas others indicated that SOTs completely fail to produce B cell responses and Abs to SARS-CoV-2 mRNA vaccines. A common denominator, however, is the heavily curtailed nAb production in SOTs following immunization. Although the evidence from studies conducted with blood samples hints at crippled GC formation, the exploration of GC responses to SARS-CoV-2 mRNA vaccination in SOTs remains uncharted territory.

Herein, by deploying a fine-needle aspiration (FNA) approach (Havenar-Daughton et al., 2020), we evaluated the GC responses elicited by SARS-CoV-2 mRNA vaccines in draining LNs of healthy donors (HDs) and kidney transplant recipients (KTXs) and assessed their connection to humoral and MBC responses. Our study uncovered a potent elicitation of SARS-CoV-2 full-length spike (Full S) and receptor binding domain (RBD)-specific GC B cells localized in vaccine-draining LNs upon primary immunization of healthy individuals, which was further enhanced by a second vaccine dose. Furthermore, SARS-CoV-2-specific GC B cell responses were associated with a robust induction of Tfh cells, class-switched RBD-specific MBCs and nAbs. These findings were in stark contrast to a profound impairment of the GC responses in KTXs, which was coupled to a nearly abolished RBD-specific memory B cell response and nAb formation, and opposed to a measurable generation of class-switched S-specific MBCs binding Full S outside the RBD region. Overall, this study shows that in individuals with an intact immune system, class-switched RBD-specific MBCs and nAbs are induced by SARS-CoV-2 mRNA vaccination and might have a GC origin. Conversely, these responses are not efficiently generated following vaccination in individuals receiving IS drugs. This work has important implications for guiding future studies aimed at unraveling human immune responses after vaccination and for supporting the decision to perform additional booster immunizations against SARS-CoV-2 in people with a compromised immune system.

RESULTS

Robust SARS-CoV-2-specific GC B cell responses are elicited by mRNA vaccines and localized in draining LNs of healthy individuals

GC B cells and Tfh cells are only present in lymphoid tissues and cannot be studied in blood (Vella et al., 2019). Hence, we conducted a human study where lymphoid tissue immune responses elicited by SARS-CoV-2 mRNA vaccines were probed in healthy individuals via FNA. The FNA approach has been successfully used to track GC B cell responses to vaccination in humans (Havenar-Daughton et al., 2020; Turner et al., 2020, 2021). In total, 15 HDs (23–76 years old) were enrolled in this study prior to vaccination with BNT162b2 or mRNA-1273 (Table S1). FNA samples were collected two weeks after the first immunization (V2: day 14+/−2) and eight days after the second immunization (V3: day 8+/−2) (Figure 1A). Matched blood samples were also obtained at the same time points and before vaccination (V1). Axillary draining LNs from the same arm where the vaccines were administered were visualized by ultrasound to guide the FNA procedure (Figure 1B). In HDs, the number of live cells recovered from FNAs ranged from 0.3 to 40 × 10^6 cells. A 23-parameter flow cytometry assay was performed on FNA samples to profile the immune responses induced by vaccination. GC B cells were defined as class-switched B cells co-expressing CD38, low-intermediate levels of CD27 and BCL6 (Figure 1C and S1A). Pre-pandemic tonsil samples, which are highly enriched in GCs, and putative quiescent cadaveric LNs from

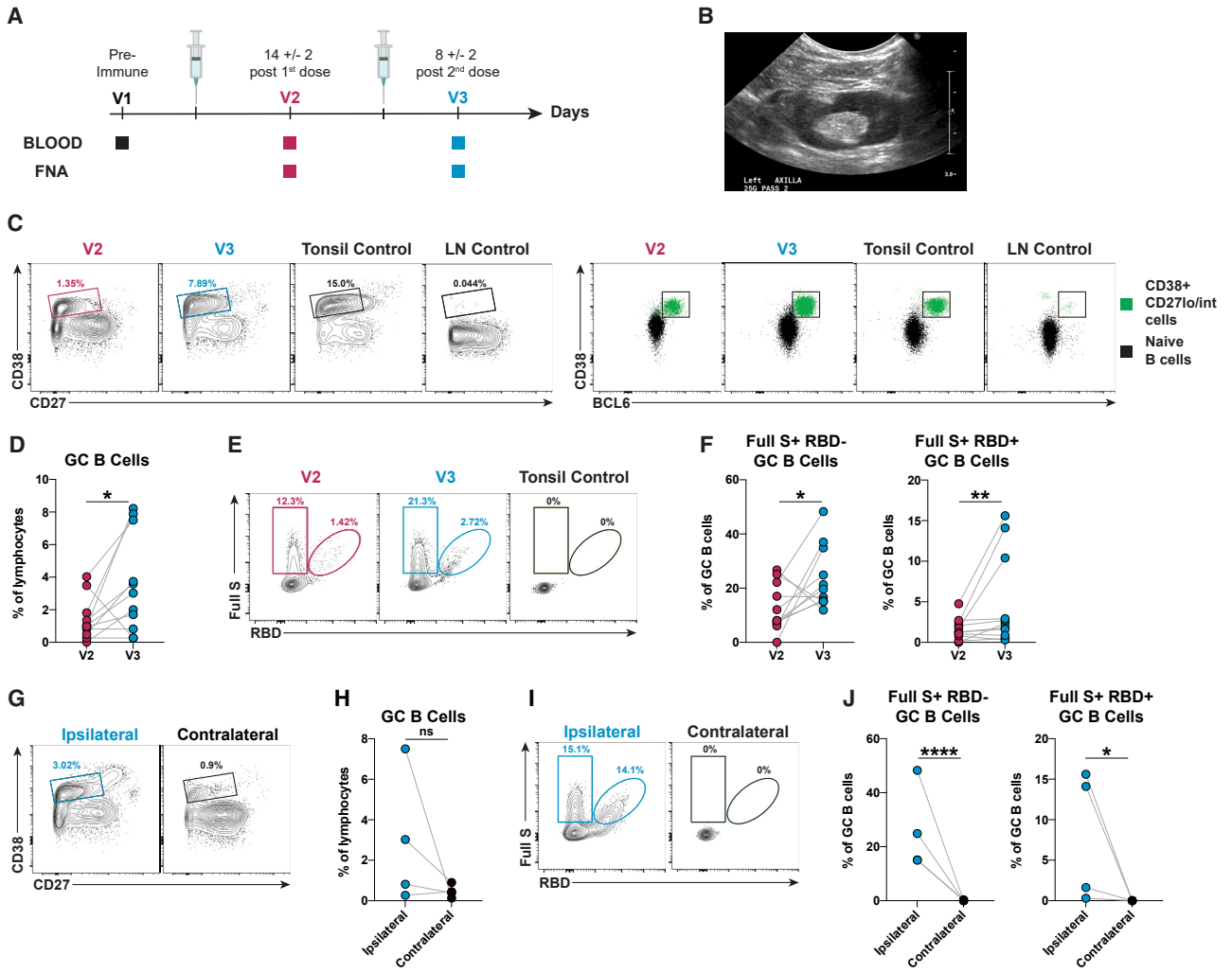

Figure 1. GC B cell responses to SARS-CoV-2 mRNA vaccines are detected in ipsilateral but not in contralateral LNs of immunocompetent individuals

(A) Schematic of study design.

(B) Representative ultrasound visualization of an HD draining axillary LN probed for the FNA procedure during V3.

(C) (Left) Representative flow cytometry plots of $CD38^{+}CD27^{lo/int}$ B cells in HD draining LNs at V2 and V3, a pre-pandemic tonsil sample (tonsil control) and a putative quiescent cadaveric LN control. (Right) Representative gating of GC B cells ($CD19^{+}CD4^{-}CD8^{-}IgM^{-}IgD^{-}CD38^{+}CD27^{lo/int}BCL6^{+}$). Naive B cells were used as negative control population to set the BCL6 gate.

(D) Quantification of GC B cells in draining LNs.

(E) Representative flow cytometry plots of SARS-CoV-2 Full S^{+} RBD^{-} and Full S^{+} RBD^{+} GC B cells ($CD19^{+}CD4^{-}CD8^{-}IgM^{-}IgD^{-}CD38^{+}CD27^{lo/int}BCL6^{+}HA^{-}$).

(F) Quantification of Full S^{+} RBD^{-} (left) and Full S^{+} RBD^{+} (right) GC B cells in draining LNs.

(G) Representative flow cytometry plots of GC B cells in draining (ipsilateral) and in nondraining (contralateral) LNs.

(H) Quantification of GC B cells in FNAs at V3 from matched ipsilateral and contralateral LNs.

(I) Representative flow cytometry plots of antigen-specific GC B cells in ipsilateral and contralateral LNs at V3.

(J) Quantification of Full S^{+} RBD^{-} (left) and Full S^{+} RBD^{+} (right) GC B cells in ipsilateral and contralateral LNs.

In (D and F), n = 11. In (H and J), n = 4. Statistical analysis: in (D and F), a paired Mann-Whitney U test with continuity correction was performed. In (H and J), the Wald-Wolfowitz runs test was performed. * $p \leq 0.05$, ** $p \leq 0.01$, **** $p \leq 0.0001$. See also Figure S1; Table S4.

SARS-CoV-2 negative individuals were used as positive and negative controls, respectively. SARS-CoV-2 mRNA vaccination elicited detectable GC B cell responses after primary immunization, which were further enhanced by the booster vaccination (Figure 1C). The increase in GC B cell frequencies was measurable when the responses were evaluated following a paired (11 individuals) or an orthogonal (15 individuals) analysis approach (Figures 1D and S1B). No correlation between age and GC B cell frequencies was observed (Figure S1C). Next, SARS-CoV-2-specific GC B cells were stratified into those binding fluorescently labeled SARS-CoV-2 Full S tetrameric probes within (Full S^{+} RBD^{+}) or outside (Full S^{+} RBD^{-}) of the RBD region,

while failing to bind an irrelevant tetrameric probe (influenza hemagglutinin, HA) (Figures 1E and S1A). The specificity of the probes is indicated by the lack of Full S- and RBD-specific GC B cells in pre-pandemic tonsils (Figure 1E). Overall, a boost in both Full S^+ RBD^- and RBD^+ GC B cell frequencies following the second vaccine dose was observed (Figures 1F and S1D). Similar to total GC B cells, SARS-CoV-2-specific GC B cells did not correlate with age (Figure S1E). Next, to determine if mRNA vaccine-induced GC responses were detectable in non-draining LNs, we collected contralateral axillary LNs, which do not directly drain the mRNA vaccines from the injection site, after the booster immunization (n = 4). When compared with the matched draining (ipsilateral) LNs, the contralateral LNs displayed a trend for lower frequencies of GC B cells (Figures 1G and 1H), which were not SARS-CoV-2-specific (Figures 1I and 1J). Overall, these data demonstrate that in immunocompetent subjects, SARS-CoV-2 mRNA vaccines efficiently elicit antigen-specific GC B cell responses that are enhanced by a booster immunization and localized in the ipsilateral draining LNs.

Tfh cell responses are detectable in draining LNs of healthy individuals upon SARS-CoV-2 mRNA vaccination

By enabling the selection of high-affinity GC B cells and curbing the magnitude of GC reactions, Tfh cells modulate affinity maturation in infection and vaccination (Crotty, 2019). We measured the frequency of GC Tfh cells (referred to as Tfh cells) defined by the signature markers CXCR5 and PD-1 (Figures 2A and S2A). Expression of the lineage-defining transcription factor BCL6 confirmed the identity of this population as Tfh cells (Figure 2B). Negligible Tfh cell frequencies were found in quiescent LNs from cadaveric donors (Figure S2B) and the contralateral LNs of vaccinees (Figure 2A), in contrast to a more abundant Tfh cell presence in tonsils (Figure S2B). The frequencies of Tfh cells in ipsilateral LNs of vaccinated HDs had a trend for higher values than that in contralateral LNs ($p = 0.056$, Figure 2C) and increased after the second vaccine dose (Figures 2D and S2C). Tfh cells are a functionally heterogenous population that, in humans, is functionally stratified by chemokine receptor expression (Ueno, 2016). CXCR3-expressing Tfh cells are Th1-polarized (Locci et al., 2013; Morita et al., 2011). By contrast, $CXCR3^-$ Tfh cells can be distinguished by CCR6 expression into Th2 ($CCR6^-$) and Th17 ($CCR6^+$)-polarized cells (Morita et al., 2011). CCR4 was also used in this analysis to help refine the delineation of Th2 ($CCR6^-CCR4^+$)- and Th17 ($CCR6^+CCR4^+$)-biased cells (Figure 2E) (Acosta-Rodriguez et al., 2007). This analysis approach showed that the Tfh cells present in the draining LNs comprised Th1- and Th2-polarized Tfh cells, but not Th17-biased Tfh cells (Figure 2F). Of note, draining LN Tfh cells correlated with both Full S^+ RBD^- GC B cells and RBD-specific GC B cells (Figure 2G), even when the outlier in the Full S^+ RBD^+ GC B cell frequency data set was excluded (data not shown, $R=0.6554$, $p=0.0003765$). While bona fide Tfh cells can be found exclusively in secondary lymphoid organs (Vella et al., 2019), a small population of circulating activated Tfh cells expressing high levels of ICOS, PD-1, and CD38 has been described in peripheral blood post vaccination (Bentebibel et al., 2013; Heit et al., 2017; Herati et al., 2014). We evaluated activated Tfh cell frequencies in peripheral blood mononuclear cell (PBMC) samples of the same HD vaccinees. The percentages of blood-activated Tfh cells ($CD4^+CD45RA^-CXCR5^+ICOS^{hi}PD\text{-}1^{hi}$), a large fraction of which also expressed CD38, were significantly increased by SARS-CoV-2 mRNA vaccination (Figures 2H and S2D) and did not correlate with bona fide Tfh cells (gated with a similar strategy) in draining LNs (Figure 2I). It is worth noting that blood Tfh cells did not correlate with the frequency of SARS-CoV-2-specific GC B cells (Figure S2E), indicating that, although reflecting the presence of an ongoing GC reaction, they are not accurate biomarkers to estimate bona fide GC B and Tfh cell responses. Hence, GC responses are best studied by direct investigation of vaccine-draining LNs.

SARS-CoV-2 mRNA vaccines lead to the generation of MBCs and plasmablasts in draining LNs of healthy subjects

As GCs are important for the generation of MBCs, we next evaluated the MBC responses elicited by SARS-CoV-2 mRNA vaccines in HDs. Class-switched MBCs were first defined as $IgD^-IgM^-CD38^-CD27^+$ B cells (Figures 3A and S1A). Since we did not include CD21 or other markers to define MBC activation status, a fraction of the cells that we defined as MBCs might still be activated. SARS-CoV-2 Full S-specific MBCs were stratified into RBD^- and RBD^+ cells (Figure 3B), as previously described for GC B cells (Figure 1E). Our analyses highlighted the generation of class-switched Full S- and RBD-specific MBCs after the first vaccine dose, which was significantly higher after a second mRNA vaccine dose (Figures 3C and S3A). Class-switched SARS-CoV-2-specific MBCs were also detectable at low frequencies in PBMC samples after two immunizations (Figure S3B). Only S-specific RBD^- MBCs in peripheral blood correlated with the respective SARS-CoV-2-specific MBC population in FNAs (Figure S3C), whereas RBD-specific MBCs did not. Low frequencies of SARS-CoV-2-specific non-class-switched IgM^+ MBCs were also present in LNs and blood and did not show a uniform increase across different locations after a second vaccine dose (Figures S3D and S3E). A population of $IgD^-IgM^-CD38^{hi}CD20^{lo/-}CD27^+BCL6^-$ plasmablasts (Figure S3F) was more abundant after the second immunization (Figure 3D) and was also detectable at variable levels in peripheral blood samples of vaccinated HDs (Figure S3G). Furthermore, SARS-CoV-2-specific plasmablasts were also increased in the draining LNs and blood after the second immunization (Figures 3E and 3F and S3H). However, no correlation was found between the total or SARS-CoV-2-specific plasmablast populations detected in FNA and blood samples (Figures S3I and S3J). In sum, the data obtained in our study indicate that two doses of SARS-CoV-2 mRNA vaccines can elicit SARS-CoV-2 S- and RBD-specific MBCs as well as a population of plasmablasts in draining LNs.

A failure to induce GC B cells by SARS-CoV-2 mRNA vaccines is associated with hindered MBC and nAb responses in kidney transplant recipients

To determine the capacity of immunocompromised individuals to form GC responses to SARS-CoV-2 mRNA vaccines, 13

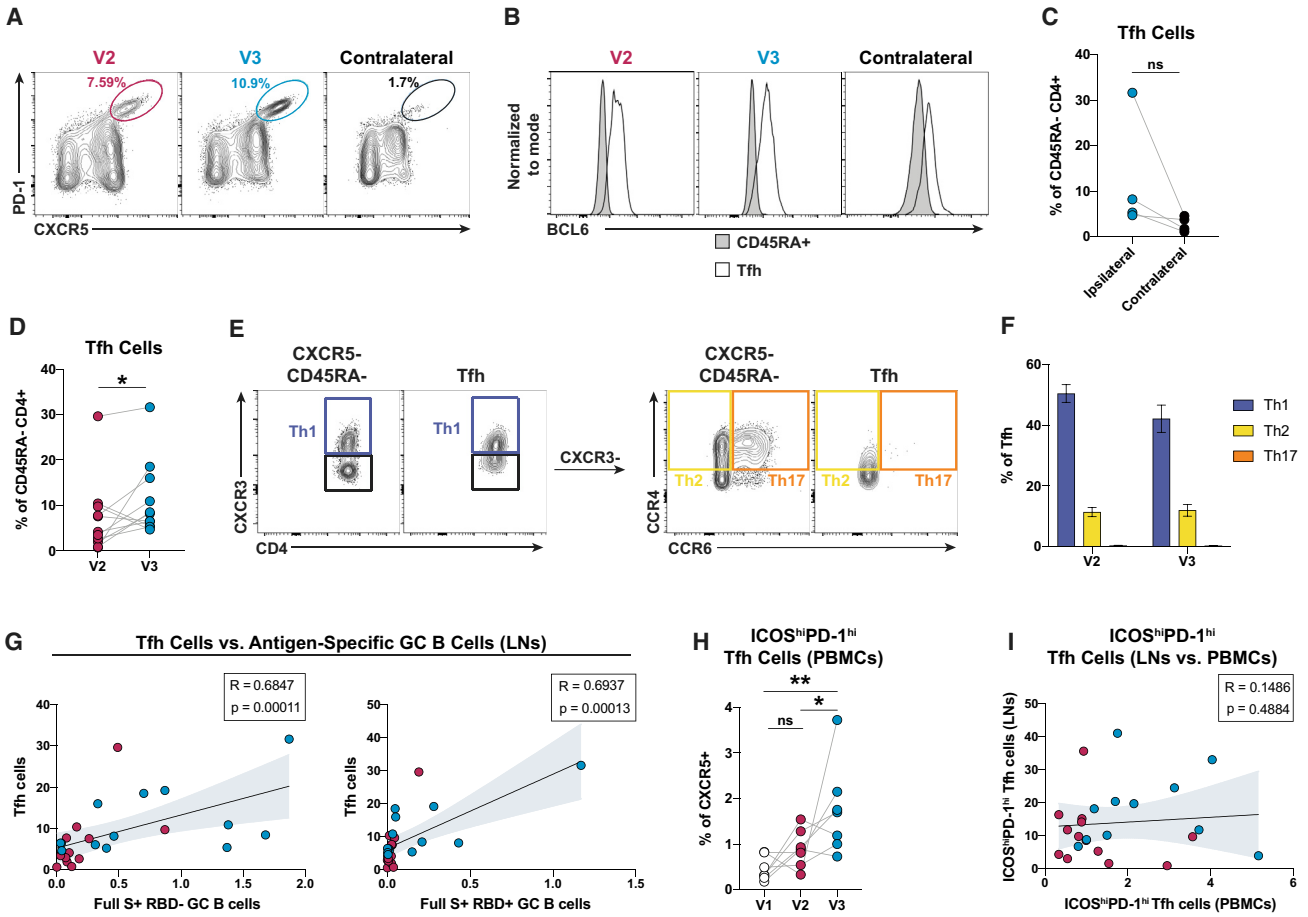

Figure 2. Tfh cell responses with a mixed Th1/Th2 profile are measurable in healthy subject LNs following immunization with SARS-CoV-2 mRNA vaccines

(A) Representative flow cytometry plots of Tfh cells ($CD4^+CD8^-CD19^-CD45RA^-CXCR5^{hi}PD\text{-}1^{hi}$).

(B) Expression of BCL6 in Tfh cells from the donors indicated in (A) is displayed as a histogram. $CD45RA^+$ CD4 T cells are used as a negative control for BCL6 expression.

(C) Quantification of Tfh cells in matched draining (ipsilateral) and nondraining (contralateral) LNs at V3.

(D) Quantification of Tfh cells in draining LNs.

(E) Representative flow cytometry plots for defining Tfh cell subsets. $CXCR5^-CD45RA^-$ (non-Tfh) were used as a control to set the chemokine receptor gates.

(F) Quantification of Tfh cell subsets displayed as a percentage of total Tfh cells from draining LNs. Tfh cells were stratified into: Th1 ($CXCR3^+$), Th2 ($CXCR3^-CCR4^+CCR6^-$), and Th17 ($CXCR3^-CCR4^+CCR6^+$).

(G) Spearman correlations between Tfh cells (displayed as a percentage of $CD45RA^-$ CD4 T cells) and SARS-CoV-2-specific GC B cells (displayed as a percentage of lymphocytes) from draining LNs at V2 (red) and V3 (blue).

(H) Quantification of activated $ICOS^{hi}PD\text{-}1^{hi}$ Tfh cells in PBMCs.

(I) Spearman correlation between activated $ICOS^{hi}PD\text{-}1^{hi}$ Tfh in PBMCs and bona fide $ICOS^{hi}PD\text{-}1^{hi}$ Tfh cells from draining LNs at V2 (red) and V3 (blue), both displayed as a percentage of $CXCR5^+$ CD4 T cells.

In (C), n = 4; in (D), n = 11; in (F and G), n = 13; in (H), n = 7; In (I), n = 11–13. In (F), data are graphed as mean ± SEM. Statistical analysis: in (D and F), a paired (D) and an unpaired (F) Mann-Whitney U test were performed. In (C and H), the Wald-Wolfowitz runs test was performed. In (G and I), correlations were determined using the Spearman's rho with a 95% confidence interval. In (G), multivariate regression analysis (where X = Tfh cells, Y_1 = Full S^+ RBD^- GC B cells, and Y_2 = Full S^+ RBD^+ GC B cells) resulted in a Benjamini-Hochberg corrected p value of 0.016. * $p \leq 0.05$, ** $p \leq 0.01$. See also Figure S2; Table S4.

KTXs were enrolled. Due to withdrawal of consent (n = 1), failure to undergo collection procedures (n = 1), and lack of sufficient cells (n = 1), 10 patients who were a median 80 days post-transplant (range −9–1,894 days) were included in further analysis (Table S1). One KTX was previously infected with SARS-CoV-2 (shown as gray square symbol). The KTXs in our cohort presented normal Ab responses established prior to transplantation, including normal levels of antigen-specific IgG induced by tetanus toxoid (TT), mumps, rubella, and measles-containing vaccines (Figures S4A–S4D). Similarly, most KTXs tested also presented detectable levels of anti-CMV (10/13) and anti-EBV (13/13) IgGs (Table S2).

After administration of SARS-CoV-2 mRNA vaccines, the FNA cell recovery yield was scarcer in KTXs (Figure S4E), making

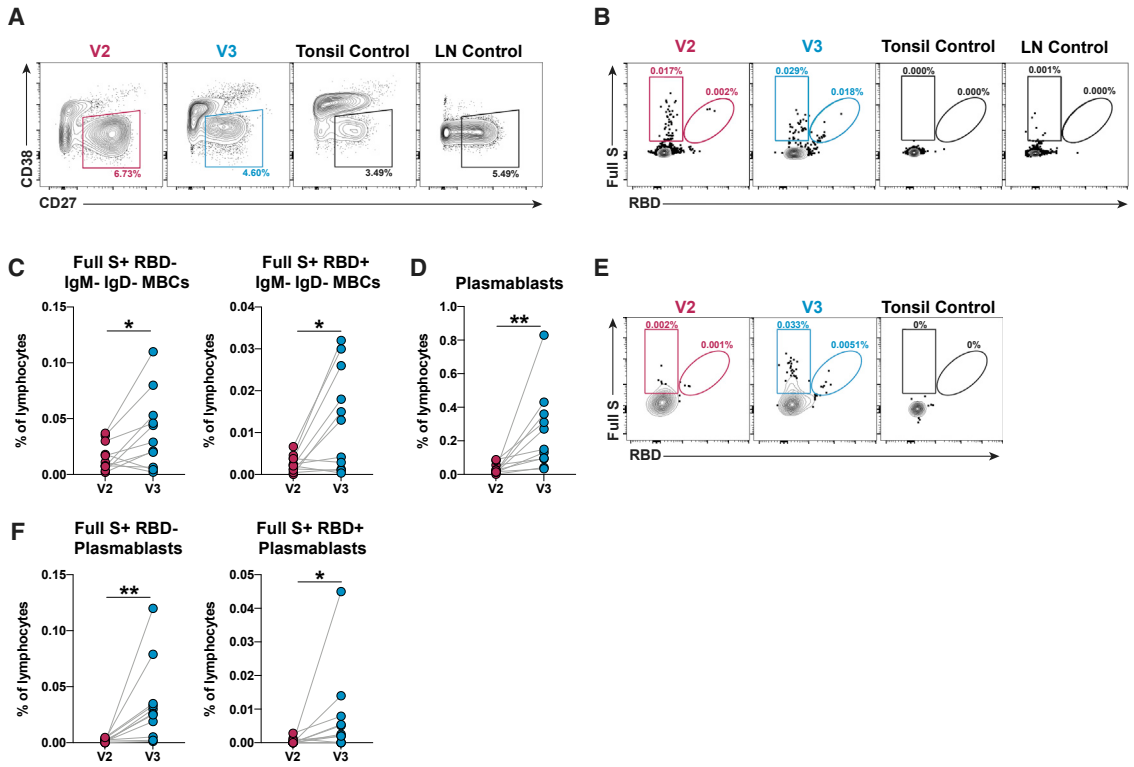

Figure 3. SARS-CoV-2 mRNA vaccinations elicit antigen-specific MBC and plasmablast responses in draining LNs of healthy individuals

(A) Representative flow cytometry of class-switched MBCs ($CD19^+CD4^-CD8^-IgM^-IgD^-CD38^-CD27^+$).

(B) Representative flow cytometry of SARS-CoV-2-specific class-switched MBCs (HA^-Full S^+RBD^- or HA^-Full S^+RBD^+).

(C) Quantification of Full S^+ RBD^- (left) and Full S^+ RBD^+ (right) class-switched MBCs in draining LNs.

(D) Quantification of plasmablasts ($CD19^+CD4^-CD8^-IgM^-IgD^-CD38^+CD20^{lo}CD27^+BCL6^-$) in draining LNs.

(E) Representative flow cytometry plots of SARS-CoV-2-specific plasmablasts (HA^-Full S^+RBD^- or HA^-Full S^+RBD^+).

(F) Quantification of Full S^+ RBD^- (left) and Full S^+ RBD^+ (right) plasmablasts in draining LNs.

In (C, D, and F), n = 11. Statistical analysis: in (C), a paired Mann-Whitney U test with continuity correction was performed. In (D and F), the Wald-Wolfowitz runs test was used to perform an exact comparison between the data distribution for V2 versus V3. * $p \leq 0.05$, ** $p \leq 0.01$. See also Figure S3; Table S4.

immunophenotyping feasible in this group only at certain time points. The class-switched B cell populations captured by our 23-color flow cytometry analysis were visualized by a dimensionality-reduction approach (Figure 4A). Of note, a large cell population, reminiscent of GC B cells ($CD38^+CD27^{lo/int}BCL6^+$) and present in immunocompetent individuals, was completely lacking in KTXs. A direct evaluation of GC B cell frequencies in KTXs further corroborated this finding and demonstrated a failure of KTXs to form GC B cell responses after one or two immunizations with SARS-CoV-2 mRNA vaccines (Figures 4B and 4C). Importantly, SARS-CoV-2-specific GC B cells induced by vaccination were completely abrogated in the few KTXs recipients who could mount low but detectable GC B cell responses (Figure 4D).

We next asked whether the failure to form SARS-CoV-2-specific GC B cells was associated with impaired MBC responses to the vaccine. SARS-CoV-2-specific MBC frequencies were determined in draining LNs and blood. Unexpectedly, the analysis of FNA samples and PBMCs from KTXs revealed a detectable frequency of class-switched Full S^+ RBD^- MBCs within total B cells after the second immunization as opposed to an almost complete lack of class-switched Full S^+ RBD^+ MBCs (Figures 4E and S4F). When analyzed as a frequency of MBCs, however, class-switched Full S^+ RBD^- MBCs were decreased in comparison to HDs (Figure S4G). These data, along with KTX-associated lymphopenia (Tables S1 and S2), indicate that KTXs respond to SARS-CoV-2 mRNA vaccine by producing detectable yet reduced levels of Full S-specific MBCs targeting regions outside the RBD. Similar to what we observed for class-switched MBCs, IgM^+ Full S^+ RBD^- but not Full S^+ RBD^+ MBCs were also detectable in draining LNs of most donors after the administration of two vaccine doses (Figure S4H). These data were only partially confirmed in blood (Figure S4I). Interestingly, when HDs and KTXs were analyzed together, a strong correlation was found between lymphoid tissue class-switched RBD-specific MBCs and GC B cells, whereas class-switched Full S^+ RBD^- MBCs and GC B cells only presented a weak correlation (Figure S4J). The correlation between class-switched RBD-specific MBCs and GC B cells remained strong after excluding the outlier data point (data not shown, R=0.8360 and p=4.077e-010). Additionally, when only HDs were analyzed, we observed similar correlations between both types of class-switched SARS-CoV-2-specific

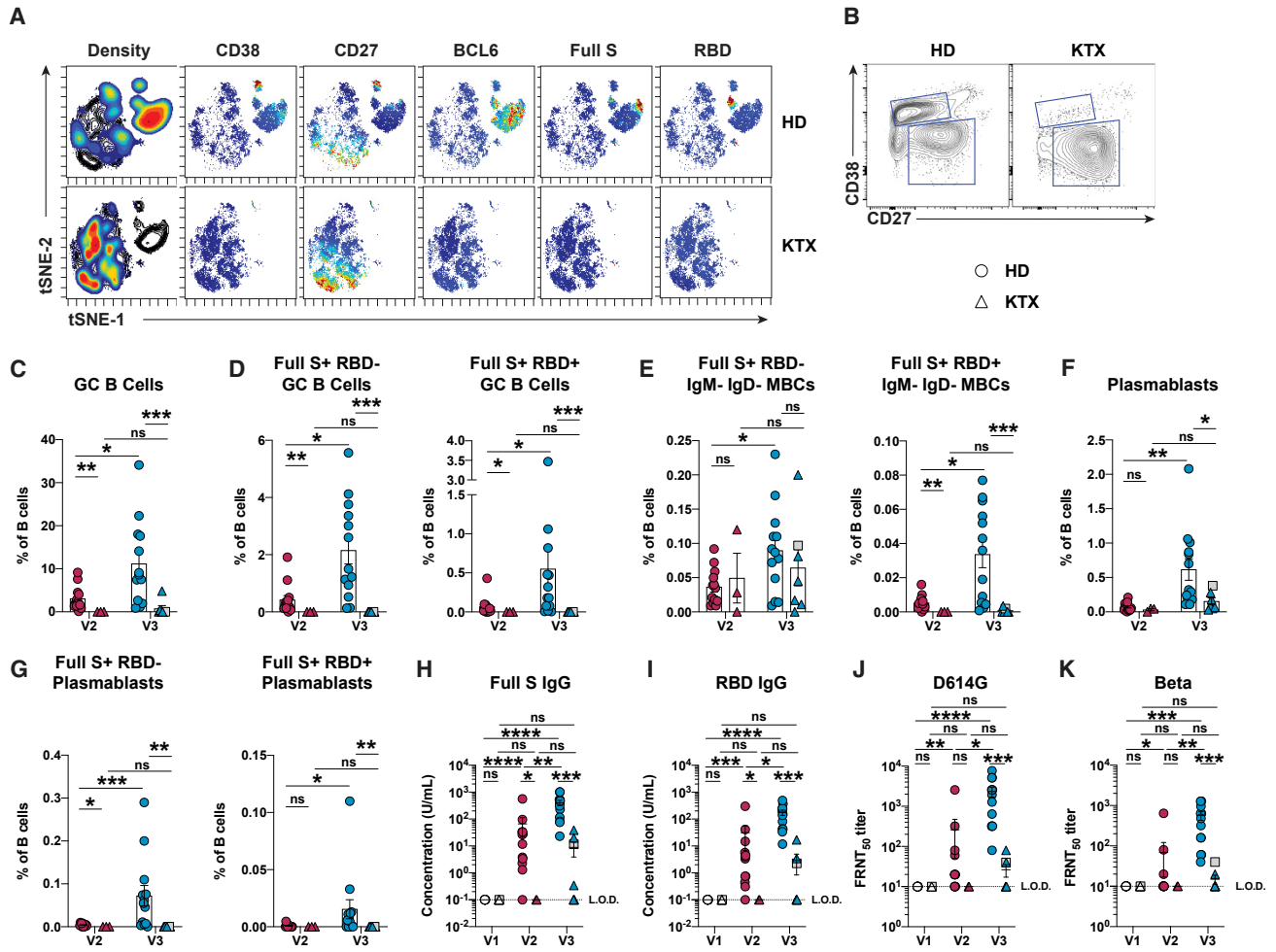

Figure 4. Kidney transplant recipients fail to mount proper GC B cell and humoral responses

(A) viSNE analysis of class-switched B cells ($CD19^+CD4^-CD8^-IgM^-IgD^-$) in draining LNs from HDs and KTXs at V3.

(B) Representative flow cytometry of GC B cells. ($CD19^+CD4^-CD8^-IgM^-IgD^-CD38^+CD27^{lo/int}BCL6^+$) in draining LNs from HDs and KTXs at V3.

(C–G) Quantification of GC B cells (C); SARS-CoV-2-specific GC B cells (D); SARS-CoV-2-specific class-switched MBCs (E); plasmablasts (F); and SARS-CoV-2-specific plasmablasts (G) in draining LNs from HDs and KTXs.

(H and I) Serum concentration of Full S-specific (H) and RBD-specific (I) IgG from HDs and KTXs measured by ELISA.

(J and K) Levels of nAbs against SARS-CoV-2 D614G (J) and Beta (K) pseudotyped viruses measured by pseudoneutralization assay in serum samples from HDs and KTXs.

In (A), for HDs and KTXs n=3. In (C–G), for HDs: n = 13; for KTXs: n = 3 at V2 and n = 7 at V3. In (H–K), for HDs: n = 12–13; for KTXs: n = 7 at V1, n = 2 at V2, and n = 8 at V3. In (C–K), circles represent HDs, triangles represent KTXs, and a gray square is used to indicate a KTX with a prior SARS-CoV-2 infection. Data are graphed as mean ± SEM. Statistical analysis: in (C–K), the Wald-Wolfowitz runs test was used to perform an exact comparison between the data distributions for HD versus KTX at each time point. * $p \leq 0.05$, ** $p \leq 0.01$, *** $p \leq 0.001$, **** $p \leq 0.0001$. See also Figures S4, S5; Table S4.

MBCs and GC B cells with the same antigen specificity (Figure S4K). Overall, these observations suggest that class-switched RBD-specific MBCs are derived from GC reactions, whereas class-switched Full S^+ RBD^- MBCs could be a mixed population with either GC-dependent or GC-independent origins.

Next, we asked whether the absence of vaccine-induced GC B cell responses in KTXs was connected to altered humoral responses, which were previously reported in a fraction of KTXs (Benotmane et al., 2021; Boyarsky et al., 2021a; Kamar et al., 2021; Massa et al., 2021; Stumpf et al., 2021). As a first step, we evaluated plasmablast frequencies after SARS-CoV-2 vaccination. Plasmablast abundance among FNAs was increased after two immunizations with SARS-CoV-2 mRNA in HDs, whereas KTX plasmablast frequencies were, for the most part, reduced in comparison to HDs (Figure 4F). Similarly, SARS-CoV-2-specific plasmablast responses in draining LNs were hindered in KTXs in comparison to HDs after a second vaccine dose (Figure 4G). Total and SARS-CoV-2-specific plasmablast responses in HDs and KTXs had less clear trends in blood (Figures S5A and S5B). A serological analysis revealed that only 3/8 of the KTXs in our FNA cohort produced Full S-

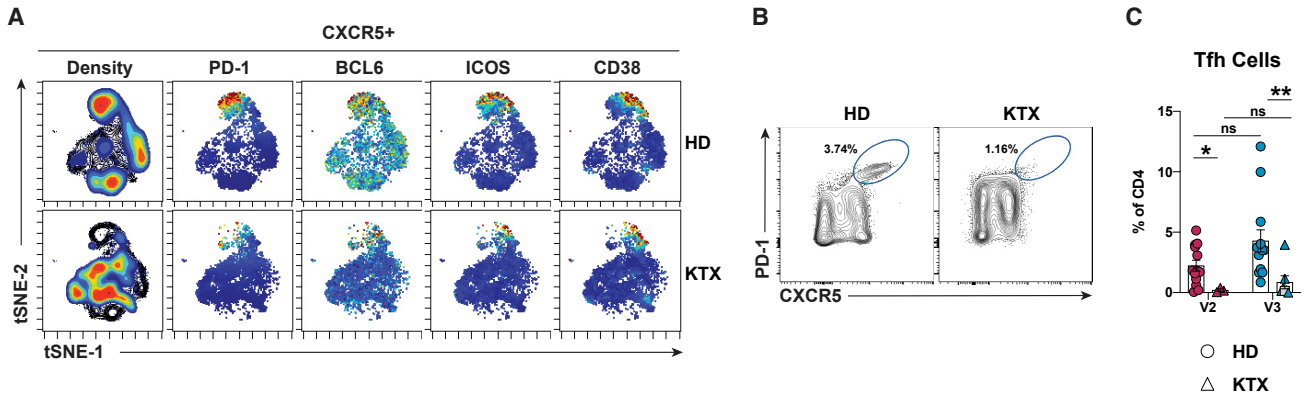

Figure 5. Tfh cell responses to mRNA vaccination are dampened in kidney transplant recipients

(A) viSNE analysis of antigen-experienced CXCR5$^+$ CD4 T cells (CD19$^-$CD8$^-$CD4$^+$CD45RA$^-$CXCR5$^+$) in draining LNs from HDs and KTXs at V3.

(B) Representative flow cytometry plots of Tfh cells (CD4$^+$CD8$^-$CD19$^-$CD45RA$^-$CXCR5^{hi}PD-1^{hi}) in draining LNs from HDs and KTXs at V3.

(C) Quantification of Tfh cells in draining LNs from HDs and KTXs.

In (A), for HDs and KTXs: n=3. In (C), for HDs: n = 13; for KTXs: n = 3 for V2 and n = 7 for V3; circles represent HDs; triangles represent KTXs; a gray square is used to indicate a KTX with a prior SARS-CoV-2 infection. In (C), data are shown as mean ± SEM. Statistical analysis: in (C), a paired Mann-Whitney U test with continuity correction was performed. * $p \leq 0.05$, ** $p \leq 0.01$. See also Table S4.

and RBD-specific IgG within the lower range of HDs after two immunizations, whereas the remaining 5/8 of the patients had SARS-CoV-2–binding Abs below the limit of detection (Figures 4H and 4I). Similar to previous data in HDs (Amanat et al., 2021), SARS-CoV-2 mRNA vaccines only modestly boosted the levels of IgG against the seasonal betacoronavirus OC43 in both HDs and KTXs (Figures S5C and S5D). Moreover, SARS-CoV-2 mRNA vaccination elicited a low yet detectable induction of SARS-CoV-2 Full S- and RBD-specific IgM and IgA in HDs, in line with other published papers (Turner et al., 2021; Wang et al., 2021a). Conversely, all KTXs presented negligible IgM and IgA production following vaccination (Figures S5E and S5F). To shed light on the quality of the Ab responses driven by SARS-CoV-2 vaccination in KTXs, we measured SARS-CoV-2 nAbs by pseudotyped lentivirus-based *in vitro* assays. In these assays, most HD samples collected after two vaccine doses could efficiently neutralize a pseudovirus containing the D614G mutation (Figure 4J) and, less efficiently, a pseudovirus containing the mutation of the SARS-CoV-2 beta strain (Figure 4K). By contrast, KTXs presented greatly diminished nAbs against D614G-pseudovirus and could not efficiently block the pseudovirus containing the SARS-CoV-2 beta strain mutations. Correlative analysis including all subjects showed that SARS-CoV-2-specific plasmablasts, binding Abs, and nAb titers in response to SARS-CoV-2 vaccination were strongly associated with the frequency of Full S$^+$ RBD$^-$ and Full S$^+$ RBD$^+$ GC B cells (Figures S5G–S5I). Moreover, while bona fide Tfh cells also displayed a positive correlation with nAb levels, blood-activated Tfh cells did not (Figure S5J). Overall, our data demonstrate that KTXs cannot mount SARS-CoV-2-specific GC B cell responses or efficiently generate RBD-specific MBCs or nAbs after administration of mRNA vaccines. Furthermore, our work points to a possible connection between GC formation, humoral responses, and RBD-specific memory B cell generation in SARS-CoV-2 vaccination.

Kidney transplant recipients fail to efficiently produce Tfh cells and SARS-CoV-2-specific T cell responses

Next, we aimed to determine whether KTXs can generate T cell responses to the vaccines. As GC B cell responses were heavily impaired in KTXs, we predicted reduced Tfh cell frequencies in the KTX group. As anticipated, a viSNE analysis of antigen-experienced CXCR5$^+$ CD4 T cells in FNA samples revealed a deep reduction of a cell population expressing the Tfh cell signature markers PD-1, BCL6, and ICOS in the KTX group (Figure 5A). Concordantly, a significant reduction of Tfh cells in KTX patients in comparison to HDs also emerged by a direct flow cytometry analysis (Figures 5B and 5C).

We then asked whether KTXs are, more broadly, incapable of mounting efficient antigen-specific T cell responses to SARS-CoV-2 mRNA vaccines. Since a direct evaluation of antigen-specific T cells in vaccine-draining LNs was not feasible due to the paucity and variability in FNA cell recovery, we measured the frequency of SARS-CoV-2-specific CD4 and CD8 T cells in peripheral blood of 11 HDs and 10 KTXs via an activation induced marker (AIM) assay following *in vitro* stimulation with a SARS-CoV-2 peptide megapool (Grifoni et al., 2020a). Similar to previous reports (Apostolidis et al., 2021; Painter et al., 2021), we detected significantly increased frequencies of AIM$^+$ (CD200$^+$CD40L$^+$) SARS-CoV-2-specific CD4 T cells in blood samples of all HDs after the first and second vaccine administration (Figures 6A and 6B and S6A). By contrast, we observed a severely reduced induction of antigen-specific CD4 T cells in KTXs after vaccination. Since KTXs might have altered ratios of naive/antigen-experienced CD4 T cells, we also analyzed the AIM$^+$ CD4 T cells as frequency of total CD4 T cells, observing a similar attenuation of SARS-CoV-2-specific CD4 T cells in the KTX group compared with HDs (Figure S6B). A functional stratification of the AIM$^+$ CD4 T cells based on chemokine receptor expression allowed us to identify SARS-CoV-2-specific circulating Tfh cells (CXCR5$^+$) and Th1 (CXCR3$^+$), Th17

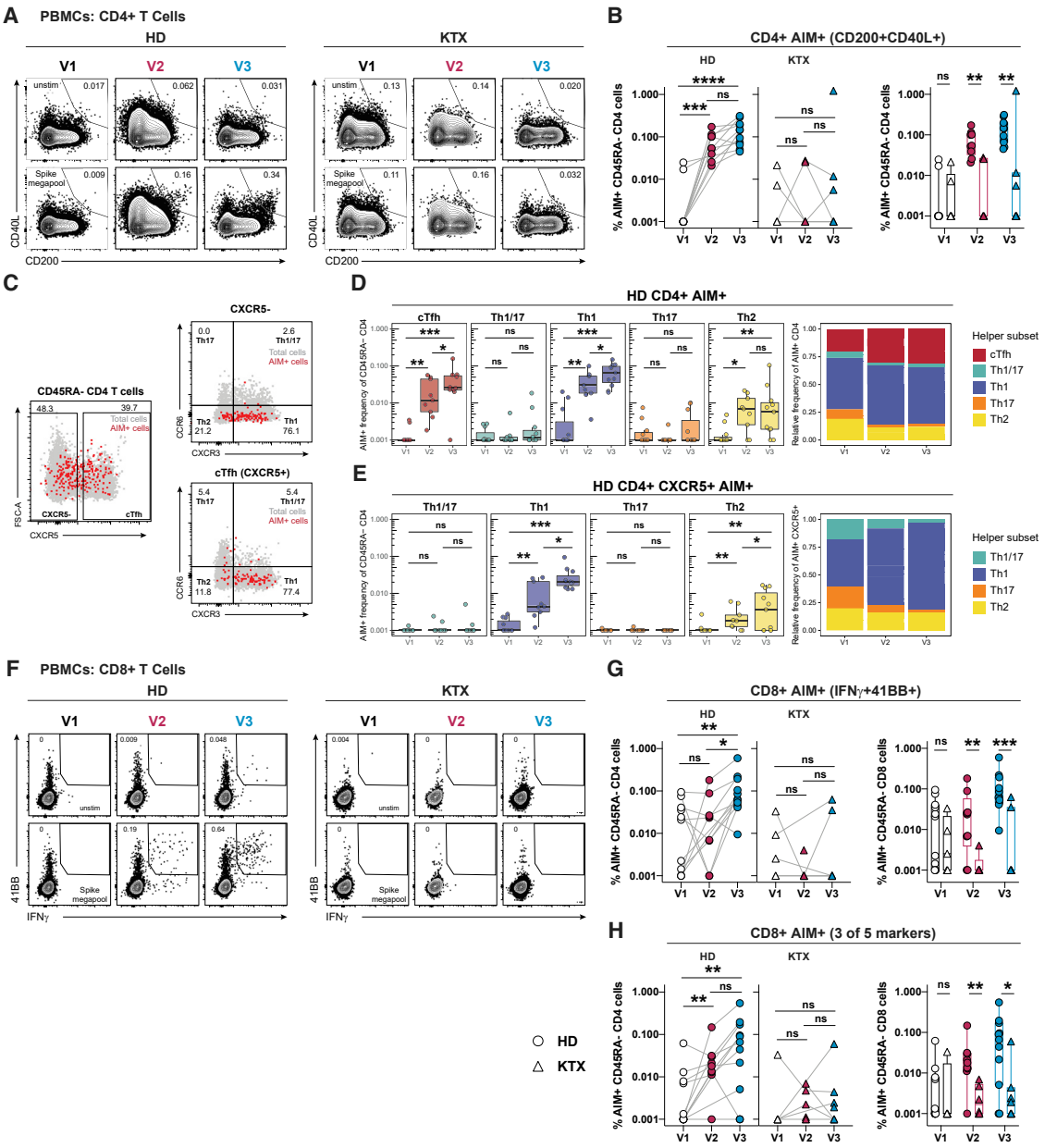

Figure 6. Kidney transplant recipients fail to generate effective antigen-specific T cell responses

(A) Representative flow cytometry plots of AIM$^+$ (CD200$^+$CD40L$^+$) CD4 T cells in PBMCs.

(B) Quantification of AIM$^+$ CD4 T cells, defined as in (A), as (left) paired or (right) unpaired analyses.

(C) Representative gating strategy to define AIM$^+$ CD4 T cell subsets in HD PBMC samples.

(D and E) Quantification of AIM$^+$ total CD4 T cell subsets (D) and AIM$^+$ CXCR5$^+$ CD4 T cell subsets (E) in HDs.

(F) Representative flow cytometry of AIM$^+$ (IFNγ$^+$ and 41BB$^+$) CD8 T cells in PBMCs.

(G and H) Quantification of AIM$^+$ (IFNγ$^+$ and 41BB$^+$) CD8 T cells (G); and AIM$^+$ (cells expressing at least 3 of 5 activation markers: CD107a, 41BB, CD200, CD40L, and IFNγ) CD8 T cells (H). Paired (left) or unpaired (orthogonal, right) analyses of PBMC samples.

In (B, D, E, G and H), for HDs: n = 9–11; for KTXs: n = 5–7. In (B) and (G–H), circles represent HDs and triangles represent KTXs. In (B, D, E, G, and H), boxplots represent median with interquartile range. Statistical analysis: in (B, D, and E), and (G and H), the Wald-Wolfowitz runs test was used to perform an exact comparison between the two data distributions of interest. * $p \leq 0.05$, ** $p \leq 0.01$, *** $p \leq 0.001$, **** $p \leq 0.0001$. See also Figure S6.

(CCR6$^+$), and Th2 (CXCR3$^-$CCR6$^-$)-polarized CXCR5$^-$ non-Tfh cells (Figure 6C) (Acosta-Rodriguez et al., 2007; Morita et al., 2011; Trifari et al., 2009). As previously observed, HDs predominantly generate SARS-CoV-2-specific circulating Tfh and Th1-polarized CD4 T cells in response to the mRNA vaccines (Figures 6C and 6D) (Apostolidis et al., 2021; Painter et al., 2021), along

with low frequencies of antigen-specific Th2-biased CD4 T cells. Of note, the SARS-CoV-2-specific circulating Tfh cells detected in HDs via the AIM assay presented a mixed Th1/Th2 functional polarization (Figure 6E), similar to what was observed in bona fide Tfh cells (Figure 2F). We did not observe alterations in the functional polarization of SARS-CoV-2-specific CD4 T cells in KTXs (Figures S6C and S6D), although the small numbers of AIM^+ CD4 T cells prevented definitive conclusions. SARS-CoV-2-specific CD8 T cells, defined either as CD8 T cells co-expressing 41BB and IFNγ or expressing 3 of 5 AIM markers used in our panel, were variable in frequency but detectable in most HDs above pre-vaccine baseline levels (Figures 6F–6H and S6E and S6F). In contrast, most KTXs did not present detectable SARS-CoV-2-specific CD8 T cells, resulting in significantly reduced responses compared with HDs (Figures 6F–6H and S6E and S6F). As opposed to the altered antigen-specific T cell responses, similar frequencies of total (non-antigen-specific) CD4 T cell subsets were found across all time points in both HDs and KTXs (Figures S6G and S6H). Although lower naive CD4 T cell frequencies could partially account for the defective CD4 T cell responses to SARS-CoV-2 mRNA vaccination, this did not appear to be the case for CD8 T cells, whose naive counterpart was grossly normal (Figures S6I and S6J). Altogether, these data point to severely decreased SARS-CoV-2-specific CD4 and CD8 T cell responses in KTXs after two immunizations with SARS-CoV-2 mRNA vaccines.

GC responses to a third dose of SARS-CoV-2 mRNA vaccines are hindered in most kidney transplant recipients

Next, we asked if KTXs failed to generate SARS-CoV-2-specific GC responses after a third dose of SARS-CoV-2 mRNA vaccine. Blood samples were collected before (V4) and after (V5) the administration of a third vaccine dose in 3/9 KTXs originally enrolled in the FNA study and in one newly enrolled KTX subject (Figure 7A). FNAs were performed on these patients at V5. In line with previous data, 3/4 KTXs presented negligible total and SARS-CoV-2-specific GC B cell frequencies after this additional booster immunization (Figures 7B–7E). While the remaining KTX had a detectable GC B cell population, most GC B cells were not able to bind the Full S and RBD probes. Tfh cell frequencies after the third immunization mostly mirrored total GC B cell frequencies (Figures 7F and 7G). Of note, an additional dose of the mRNA vaccines resulted in a trend for increased percentages of class-switched Full S^+ RBD^- but not Full S^+ RBD^+ MBCs in the KTX group (Figures 7H and 7I), indicating that the Full S^+ RBD^- memory B cell population is responsive to SARS-CoV-2 mRNA vaccines. SARS-CoV-2–binding and SARS-CoV-2–neutralizing Abs were also measured before and after this additional booster dose on the 3 KTXs that were originally part of the FNA study cohort. All KTXs tested displayed a trend for mildly increased Full S binding IgG responses at V5 (Figure 7J). By contrast, only 1/3 KTX (Donor 014), which already presented some RBD-binding IgG and nAbs at V3, had detectable levels of RBD-binding IgG (Figure 7K) and nAbs against a pseudovirus carrying the D614G or the mutations of SARS-CoV-2 beta variant (Figures 7L and 7M). Overall, these data suggest that while most KTXs lack the ability of mounting GC responses to additional booster doses of mRNA vaccines, they all present variable but trending increased Full S binding IgG levels and class-switched Full S^+ RBD^- memory B cell frequencies after a third vaccine dose.

DISCUSSION

mRNA vaccines are a novel vaccine platform that has only been recently approved for human use during the current coronavirus disease 2019 (COVID-19) pandemic. Although it is emerging that SARS-CoV-2 mRNA vaccines are highly efficient at inducing robust nAbs and MBC responses, a fundamental open question is whether nAb and MBC generation during SARS-CoV-2 mRNA vaccination is connected to the formation of GCs, microanatomical structures canonically harboring the generation of affinity matured Ab-secreting cells and certain MBCs. The study of vaccine-induced GC reactions in humans is heavily constrained when blood, the most easily obtainable human material, is the only available sample because bona fide GC B cells and Tfh cells are only present in secondary lymphoid organs (Vella et al., 2019). Surrogate biomarkers such as blood CXCL13 and circulating activated Tfh cells have been used thus far to predict the magnitude of ongoing GC responses (Havenar-Daughton et al., 2016; Vella et al., 2019). However, these biomarkers present significant shortcomings when trying to directly assay GC responses. They are traceable for only short windows of time, are not detectable in all individuals, and have not been successfully used to predict broad qualitative aspects of GC reactions, such as the antigen specificity of GC B cells and their connection to GC-derived B cell responses (Bentebibel et al., 2013; Havenar-Daughton et al., 2016). These limitations emphasize the need for directly probing GC responses by adopting minimally invasive approaches, such as FNA, that allow longitudinal sampling of the vaccine-draining LNs. Only two peer-reviewed studies have ever described human GC responses to vaccination (against influenza or SARS-CoV-2) in humans by using FNA (Turner et al., 2020, 2021). One study (Turner et al., 2021) reported S-specific GC B cell responses to SARS-CoV-2 mRNA vaccination in LNs but did not investigate the generation of RBD-specific GC B cells or the connection between SARS-CoV-2-specific GC B cells and Tfh cells, nAbs, and SARS-CoV-2-specific MBCs. Our study sought to address these open questions and revealed that these vaccines prompted the formation of robust Full S- and RBD-specific GC B cell and Tfh cell responses localized in draining axillary LNs. Importantly, our study revealed that SARS-CoV-2-specific GC B cell populations were strongly associated with the ability to produce SARS-CoV-2 nAbs, as further supported by the evidence that immunosuppressed individuals, who cannot form GCs, presented deeply blunted nAb production. Although to a lower degree, we also found that bona fide Tfh cells in draining LNs correlated with nAb production, whereas activated Tfh cells in blood were a less reliable predictor of nAb generation. Additionally, in our study, GC formation appeared to be tightly connected with the capacity to produce class-switched RBD-specific MBCs. These findings provide valuable insights on the otherwise poorly understood processes by which nAbs and MBCs are formed in humans after immunization with SARS-CoV-2 mRNA vaccines.

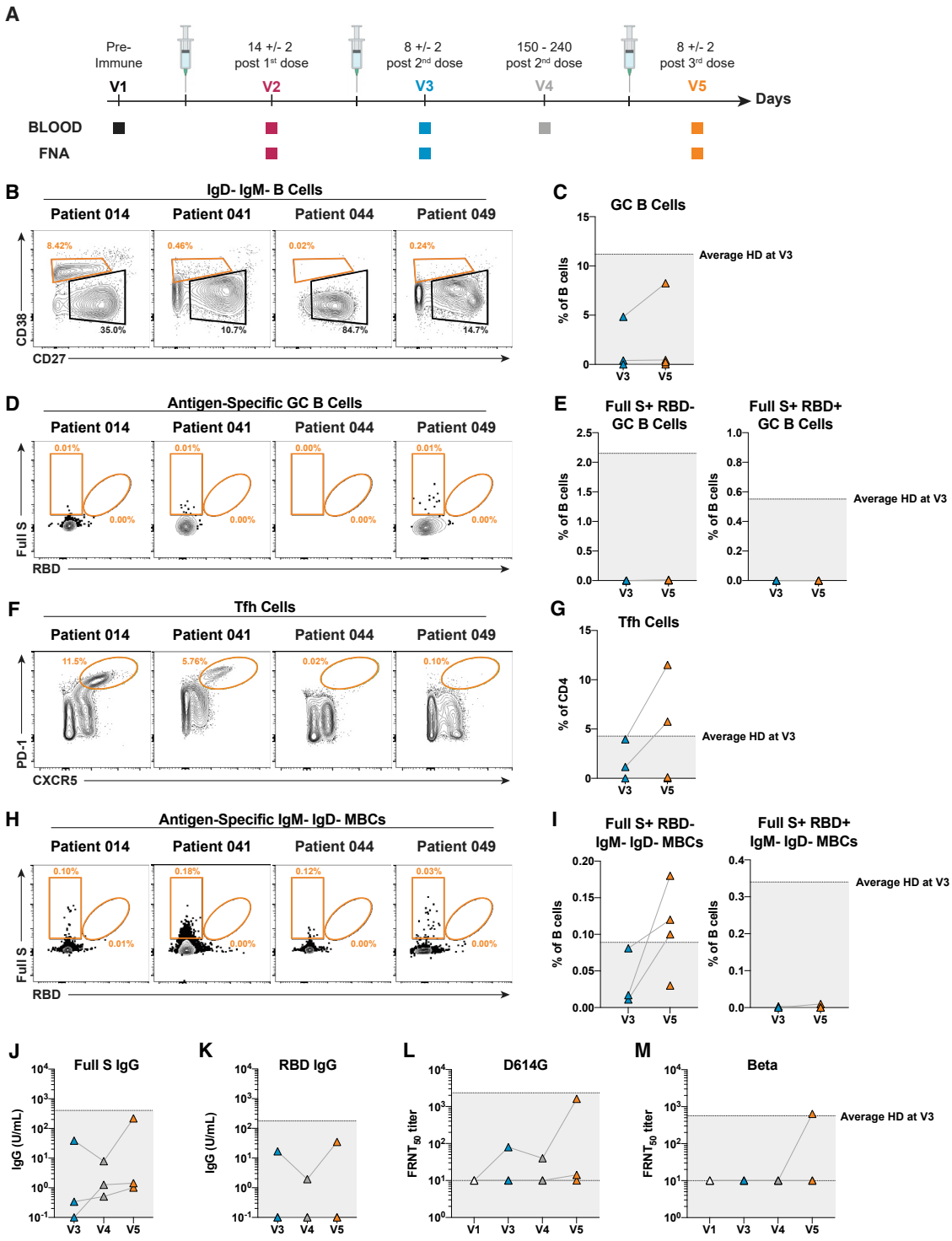

Figure 7. A third vaccine dose expands Full S$^+$ RBD$^-$ MBCs but does not induce antigen-binding GCs in kidney transplant recipients

(A) Schematic of study design including third doses.

(B) Flow cytometry plots of GC B cells (CD19$^+$CD4$^-$CD8$^-$IgM$^-$IgD$^-$CD38$^+$CD27$^{lo/int}$BCL6$^+$) and MBCs (CD19$^+$CD4$^-$CD8$^-$IgM$^-$IgD$^-$CD38$^-$CD27$^+$) at V5.

(C) Quantification of GC B cells in KTX draining LNs. Paired (n=3) and unpaired (n=1) samples from V3 and/or V5 are shown.

(D) Flow cytometry plots of SARS-CoV-2 Full S$^+$ RBD$^-$ and Full S$^+$ RBD$^+$ GC B cells in KTXs at V5.

(E) Quantification of Full S$^+$ RBD$^-$ (left) and Full S$^+$ RBD$^+$ (right) GC B cells in KTX draining LNs. Paired (n = 3) and unpaired (n = 1) samples from V3 and/or V5 are shown.

(legend continued on next page)

SARS-CoV-2-specific Abs, including nAbs, play a key role in the protection against COVID-19, in animal models (McMahan et al., 2021; Rogers et al., 2020; Zost et al., 2020) and humans (Bergwerk et al., 2021; Earle et al., 2021; Khoury et al., 2021; Lumley et al., 2021). The strong association between SARS-CoV-2-specific GC B cells and nAbs reported by our study, which recapitulates our previous observation in mice (Lederer et al., 2020), suggests that GC responses are critical to mount a SARS-CoV-2 nAb response during vaccination. However, despite robust evidence that affinity maturation (hence GC responses) can occur in COVID-19 convalescent patients after infection (Muecksch et al., 2021; Wang et al., 2021b), the reliance on GC formation for nAb production appears less overt in natural infection. Multiple groups reported that several near-germline nAbs, endowed with potent *in vitro* neutralizing activity, are elicited during natural SARS-CoV-2 infection in humans (Brouwer et al., 2020; Kreer et al., 2020; Schultheiß et al., 2020; Seydoux et al., 2020). The low degree of SHM of these Abs is suggestive of a limited GC process involved in their generation. Similarly, Tfh cell-deficient mice, which form negligible GCs in response to SARS-CoV-2 infection, mounted a decreased yet detectable production of nAbs (Chen et al., 2021). Overall, these data indicate that GCs might not be necessary to generate nAbs in response to infection. This apparently discordant outcome might stem from a combination of diverse factors, including a different pool of germline B cells recruited by SARS-CoV-2 mRNA vaccination not recruited during natural infection. Both BNT162b2 and mRNA-1273 vaccines encode for a prefusion stabilized version of the Full S protein (Wrapp et al., 2020), which induces nAbs that bind more broadly across the RBD in comparison to infection-induced nAbs (Greaney et al., 2021). This suggests that additional/alternative germline precursors of the nAb secreting cells are recruited by SARS-CoV-2 mRNA vaccines. It is tempting to speculate that some of these nAb precursors require GC reactions to produce high-affinity nAbs, as supported by the high levels of SHM in mRNA vaccine-induced plasmablasts (Amanat et al., 2021). As an alternative explanation for the GC-nAb connection, the mRNA vaccine platform might favor the formation of GC-derived nAbs—thanks to its strong pro-GC activity. We and others have shown that the mRNA vaccines are very effective at inducing GC reactions in animal models (Lederer et al., 2020; Lindgren et al., 2017; Pardi et al., 2018a), with a mechanism that relies on an early induction of the pro-Tfh cytokine IL-6 by the lipid nanoparticle component (Alameh et al., 2021). The present study, along with published work (Turner et al., 2021), further extend our earlier observation (Lederer et al., 2020) by directly showing the formation of SARS-CoV-2-specific GC B cells in humans after mRNA vaccination. Hence, by eliciting effective GC responses and/or potentially recruiting nAb precursors that can seed GCs, SARS-CoV-2 mRNA vaccines might mechanistically rely on GC responses to effectively generate nAbs.

The second part of our study was aimed at evaluating the GC responses in KTXs and their association with humoral and MBC responses, as no study has ever evaluated B cell responses in vaccine-draining lymphoid tissue of immunocompromised individuals. In agreement with studies reporting that a fraction of KTXs can produce SARS-CoV-2–binding Abs after two immunizations with SARS-CoV-2 mRNA (Benotmane et al., 2021; Boyarsky et al., 2021a; Kamar et al., 2021; Massa et al., 2021; Stumpf et al., 2021), we observed that 3/8 KTXs enrolled in our FNA study produced Full S- and RBD-specific IgG after two vaccine doses, albeit within the lower range of healthy controls. Of note, in KTXs, we also found reduced, yet detectable, vaccine-induced SARS-CoV-2-specific MBCs targeting the Full S protein outside the RBD region. Nonetheless, we reported a complete failure of KTXs in forming SARS-CoV-2-specific GC B cell responses after the administration of two mRNA vaccine doses. This finding was accompanied by a markedly diminished generation of RBD-specific MBCs and SARS-CoV-2 nAbs, suggesting that a defective GC formation to mRNA vaccination could be the underlying culprit. Given their suboptimal B cell responses following vaccination, an important question is whether mRNA vaccines are capable of eliciting T cell responses in KTXs. In immunocompetent subjects, the licensed mRNA vaccines predominantly promote the formation of circulating blood Tfh cells and Th1-polarized CD4 T cells (Painter et al., 2021). KTXs were almost completely deprived of lymph node Tfh cells after SARS-CoV-2 mRNA vaccination, which is consistent with the lack of GC B cell formation in these patients. In line with other studies (Sattler et al., 2021; Stumpf et al., 2021), SARS-CoV-2-specific CD4 (including circulating Tfh cells and Th1-polarized cells) and CD8 T cell populations in peripheral blood were also decreased in frequency in KTXs when compared with the HDs. Overall, our study indicates that while some residual immune response is obtainable by SARS-CoV-2 mRNA vaccination, B and T cell responses appear to be quantitatively and qualitatively curtailed in KTXs after two mRNA vaccine doses. Since a third vaccine dose can significantly boost SARS-CoV-2 binding Abs and nAbs in some SOTs (Hall et al., 2021; Kamar et al., 2021; Massa et al., 2021), we assessed the immune responses to an additional injection of mRNA vaccines in a small number of KTXs. This third vaccine dose did not induce GC B cell responses in 3/4 KTXs evaluated. However, it was accompanied by an upward trend in Full S-specific IgG levels and class-switched Full S^+ RBD^- MBC frequencies, which varied in

(F) Flow cytometry plots of Tfh cells in KTXs at V5.
(G) Quantification of Tfh cells in KTX draining LNs. Paired (n = 3) and unpaired (n = 1) samples from V3 and/or V5 are shown.
(H) Flow cytometry plots of class-switched SARS-CoV-2 Full S^+ RBD^- and Full S^+ RBD^+ MBCs in KTXs at V5.
(I) Quantification of class-switched Full S^+ RBD^- (left) and Full S^+ RBD^+ (right) MBCs in KTX draining LNs. Paired (n = 3) and unpaired (n = 1) samples from V3 and/or V5 are shown.
(J and K) Serum concentration of Full S-specific (J) and RBD-specific (K) IgG from KTXs measured by ELISA.
(L and M) Levels of nAbs against SARS-CoV-2 D614G (L) and Beta (M) pseudotyped viruses measured by pseudoneutralization assays in serum samples from HDs and KTXs.
In (C, E, G, I, and J–M), dotted line represents the average of HD responses at V3. In (C, E, G, and I) n = 3 for V3 and n = 4 for V5. In (J–M), n = 3 for all visits plotted. Statistical analysis was not performed for the data reported in this figure due to the small sample size of the groups.

magnitude. Although it will be important to further corroborate these finding in larger follow-up studies, these data hint at the possibility that additional booster immunizations with SARS-CoV-2 mRNA vaccines target and expand, in most KTXs, a small pool of Full S^+ RBD^- MBCs rather than promoting the *de novo* generation of Abs via GC reactions.

Suboptimal vaccine responses in organ transplant subjects receiving IS drugs were previously reported for other vaccines including influenza A/H1N1 and Hepatitis B (Brakemeier et al., 2012; Broeders et al., 2011; Cowan et al., 2014; Elhanan et al., 2018; Friedrich et al., 2015). Collectively, these studies reported impaired Ab production post vaccination. The heavily diminished induction of GC B cells, MBCs, and nAbs in KTXs observed in this study might result from the lack of adequate T cell help and by intrinsic B cell dysfunction caused by IS drugs. KTXs in this study uniformly received ATG to induce T cell depletion at the time of kidney transplantation (completed within a week) (Mohty, 2007). Hence, an incomplete reconstitution of the T cell pool might at least partially explain the hampered Tfh and SARS-CoV-2-specific T cell responses in KTXs, as potentially indicated by their lymphopenic status and deeply blunted frequencies of naive CD4 T cells. Additionally, maintenance immunosuppression is comprised of prednisone, a calcineurin inhibitor, and an antimetabolite, which have been shown to broadly dampen TCR signaling and T cell metabolism, expansion, and/or function (Flanagan et al., 1991; Liu et al., 1991; Otsuka et al., 2021; Quéméneur et al., 2002; Taves and Ashwell, 2021; Vaeth et al., 2017) and can contribute to the global T cell dysfunction of KTXs. Knowledge of the impact of the IS on Tfh cell biology in the GC is still limited, with sporadic evidence suggesting that certain IS such as calcineurin inhibitors might influence the differentiation and function of Tfh cells (Wallin et al., 2018). Altogether, these findings suggest that the lack of proper Tfh cell differentiation and T cell help to B cells might constitute a major obstacle to the development of effective GC B cell responses in immunosuppressed individuals. Additionally, IS drugs could intrinsically hinder B cell capacity to become activated and initiate GC B cell responses, as suggested by published studies indicating that certain drugs, such as antimetabolites, directly suppress B cell proliferation and plasma cell differentiation (Eickenberg et al., 2012; Karnell et al., 2011).

In sum, by directly probing GC responses at their source, we provided an informative perspective on the connection between GC formation and nAb/MBC generation following immunizations with SARS-CoV-2 mRNA vaccines in healthy and immunocompromised individuals. Broadly, this work will pave the road to future human vaccine studies aimed at untangling the origin of long-lasting, protective immune responses after immunizations with different licensed vaccines.

Limitations of the study

Due to the challenge of enrolling participants in FNA studies in a timely fashion, the HD and KTX groups in our study were not perfectly matched for ethnicity, age, and gender. Thus far, despite an outstanding SARS-CoV-2 mRNA vaccine efficacy in different demographic groups that could be suggestive of largely comparable immune responses to the vaccine (Baden et al., 2020; Polack et al., 2020), a direct comparison of GC responses between demographic groups has not been performed. Although a profound defect in GC responses, such as the one described in the KTX group, is unlikely to be entirely dependent on the variables listed above, larger confirmatory studies with a more balanced control of ethnicity, age, and gender will be important to strengthen our findings.

Another aspect that was not possible to elucidate in our study, due to the paucity of available biospecimens, is whether the Full S^+ RBD^- MBCs that are present in KTXs following SARS-CoV-2 mRNA vaccination are pre-existing MBCs specific for seasonal human coronaviruses. These MBCs could indeed have been generated before the KTXs became immunocompromised and might potentially have some degree of cross-reactivity with SARS-CoV-2 S protein that could lead to their expansion upon repeated administrations of the SARS-CoV-2 mRNA vaccines. Future studies will be needed to determine the origin of these cells as well as the role that they might play in conferring protection from COVID-19.

STAR★METHODS

Detailed methods are provided in the online version of this paper and include the following:

- KEY RESOURCES TABLE
- RESOURCE AVAILABILITY
  - Lead contact
  - Materials availability
  - Data and code availability
- EXPERIMENTAL MODEL AND SUBJECT DETAILS
  - Study design and human samples
- METHOD DETAILS
  - Ultrasound guided fine needle aspiration
  - Blood processing
  - Production of fluorescently labeled proteins
  - Flow cytometry
  - viSNE analysis
  - Activation-induced marker expression assay
  - Enzyme-linked immunosorbent assay
  - Pseudovirus neutralization assay
- QUANTIFICATION AND STATISTICAL ANALYSIS

SUPPLEMENTAL INFORMATION

Supplemental information can be found online at https://doi.org/10.1016/j.cell.2022.01.027.

ACKNOWLEDGMENTS

M.L. was supported by NIH NIAID grants R01 AI123738 and R01AI153064. This work was funded by the Gift of Life Transplant Foundation (V.B. and A.N.), the National Blood Foundation (V.B.), the Burroughs Wellcome Fund (V.B.), the U19AI082630 (S.E.H. and E.J.W.), and the NIH NIAID under contract Nr. 75N9301900065 (D.W. and A.S.). The authors wish to thank all of the subjects for their participation in this study. We also thank Dr. Fatima Amanat and Dr. Florian Krammer for kindly providing the RBD protein used in this study, Diane Mclaughlin and Sarah Benchimol for administrative assistance, Susan Rostami for assistance with sample processing, and Nicole Tanenbaum for assistance with ELISAs. We thank Dr. Florin Tuluc and Jennifer Murray of the CHOP Flow cytometry core facility for technical assistance and the flow

cytometry Core at the University of Pennsylvania. The graphical abstract was created with BioRender.com.

AUTHOR CONTRIBUTIONS

K.L., E.B., D.C., and M.L. performed and/or analyzed the immunophenotyping of FNA and blood samples. M.P., K.P., and R.R.G. performed and/or analyzed AIM assays. D.A. performed statistical analysis. K.A.L. and P.B. performed and/or analyzed the neutralization assays. M.W., K.M., E.M.D., S.G., J.T.O., M.A., and S.E.H. performed and/or analyzed serological data. X.X. processed blood samples. A.R.G. provided support with Cytobank analysis. C.L.C. and N.R. provided tonsil samples. L.J. and M.R. shared expertise for FNA procedures. D.W. and A.S. provided SARS-CoV-2 peptide mega pools. J.T.-C. and G.M. provided regulatory support. A.N., M.K., B.B., V.B., and K.P. supervised the recruitment of the subjects involved in the study as well as FNA and blood sample collection. M.L. wrote the manuscript with help from K.L., E.B., and V.B. and input from the other authors. M.L. conceived and supervised the study with support from E.J.W., A.N., and V.B.

DECLARATION OF INTERESTS

E.J.W. is consulting or is an advisor for Merck, Elstar, Janssen, Related Sciences, Synthekine, and Surface Oncology. E.J.W. is a founder of Surface Oncology and Arsenal Biosciences. E.J.W. is an inventor on a patent (US Patent number 10,370,446) submitted by Emory University that covers the use of PD-1 blockade to treat infections and cancer. S.E.H. has received consultancy fee from Sanofi Pasteur, Lumen, Novavax, and Merck for work unrelated to this report. A.S. is a consultant for Gritstone, Flow Pharma, Arcturus, Immunoscape, CellCarta, Oxford Immunotech, and Avalia.

Received: August 24, 2021
Revised: December 13, 2021
Accepted: January 28, 2022
Published: February 2, 2022

REFERENCES

Acosta-Rodriguez, E.V., Rivino, L., Geginat, J., Jarrossay, D., Gattorno, M., Lanzavecchia, A., Sallusto, F., and Napolitani, G. (2007). Surface phenotype and antigenic specificity of human interleukin 17-producing T helper memory cells. Nat. Immunol. *8*, 639–646.

Alameh, M.-G., Tombácz, I., Bettini, E., Lederer, K., Sittplangkoon, C., Wilmore, J.R., Gaudette, B.T., Soliman, O.Y., Pine, M., Hicks, P., et al. (2021). Lipid nanoparticles enhance the efficacy of mRNA and protein subunit vaccines by inducing robust T follicular helper cell and humoral responses. Immunity *54*, 2877–2892.e7.

Allen, C.D.C., Okada, T., and Cyster, J.G. (2007). Germinal-center organization and cellular dynamics. Immunity *27*, 190–202.

Amanat, F., Stadlbauer, D., Strohmeier, S., Nguyen, T.H.O., Chromikova, V., McMahon, M., Jiang, K., Arunkumar, G.A., Jurczyszak, D., Polanco, J., et al. (2020). A serological assay to detect SARS-CoV-2 seroconversion in humans. Nat. Med. *26*, 1033–1036.

Amanat, F., Thapa, M., Lei, T., Ahmed, S.M.S., Adelsberg, D.C., Carreño, J.M., Strohmeier, S., Schmitz, A.J., Zafar, S., Zhou, J.Q., et al. (2021). SARS-CoV-2 mRNA vaccination induces functionally diverse antibodies to NTD, RBD, and S2. Cell *184*, 3936–3948.e10.

Anderson, E.M., Eilola, T., Goodwin, E., Bolton, M.J., Gouma, S., Goel, R.R., Painter, M.M., Apostolidis, S.A., Mathew, D., Dunbar, D., et al. (2021a). SARS-CoV-2 infections elicit higher levels of original antigenic sin antibodies compared to SARS-CoV-2 mRNA vaccinations. medRxiv.

Anderson, E.M., Goodwin, E.C., Verma, A., Arevalo, C.P., Bolton, M.J., Weirick, M.E., Gouma, S., McAllister, C.M., Christensen, S.R., Weaver, J., et al. (2021b). Seasonal human coronavirus antibodies are boosted upon SARS-CoV-2 infection but not associated with protection. Cell *184*, 1858–1864.e10.

Apostolidis, S.A., Kakara, M., Painter, M.M., Goel, R.R., Mathew, D., Lenzi, K., Rezk, A., Patterson, K.R., Espinoza, D.A., Kadri, J.C., et al. (2021). Altered cellular and humoral immune responses following SARS-CoV-2 mRNA vaccination in patients with multiple sclerosis on anti-CD20 therapy. medRxiv.

Awasthi, S., Hook, L.M., Pardi, N., Wang, F., Myles, A., Cancro, M.P., Cohen, G.H., Weissman, D., and Friedman, H.M. (2019). Nucleoside-modified mRNA encoding HSV-2 glycoproteins C, D, and E prevents clinical and subclinical genital herpes. Sci. Immunol. *4*, eaaw7083.

Baden, L.R., Sahly, H.M.E., Essink, B., Kotloff, K., Frey, S., Novak, R., Diemert, D., Spector, S.A., Rouphael, N., Creech, C.B., et al. (2020). Efficacy and safety of the mRNA-1273 SARS-CoV-2 vaccine. N. Engl. J. Med. *384*, 403–416.

Benjamini, Y., and Hochberg, Y. (1995). Controlling the false discovery rate: A practical and powerful approach to multiple testing. J. R. Stat. Soc. B *57*, 289–300.

Benotmane, I., Gautier, G., Perrin, P., Olagne, J., Cognard, N., Fafi-Kremer, S., and Caillard, S. (2021). Antibody response After a third dose of the mRNA-1273 SARS-CoV-2 vaccine in kidney transplant recipients With minimal serologic response to 2 doses. JAMA *326*, 1063–1065.

Bentebibel, S.E., Lopez, S., Obermoser, G., Schmitt, N., Mueller, C., Harrod, C., Flano, E., Mejias, A., Albrecht, R.A., Blankenship, D., et al. (2013). Induction of ICOS+CXCR3+CXCR5+ TH cells correlates with antibody responses to influenza vaccination. Sci. Transl. Med. *5*, 176ra32.

Bergwerk, M., Gonen, T., Lustig, Y., Amit, S., Lipsitch, M., Cohen, C., Mandelboim, M., Levin, E.G., Rubin, C., Indenbaum, V., et al. (2021). Covid-19 breakthrough infections in vaccinated health care workers. N. Engl. J. Med. *385*, 1474–1484.

Bettini, E., and Locci, M. (2021). SARS-CoV-2 mRNA vaccines: immunological mechanism and beyond. Vaccines (Basel) *9*, 147.

Boyarsky, B.J., Werbel, W.A., Avery, R.K., Tobian, A.A.R., Massie, A.B., Segev, D.L., and Garonzik-Wang, J.M. (2021a). Antibody response to 2-dose SARS-CoV-2 mRNA vaccine series in solid organ transplant recipients. JAMA *325*, 2204–2206.

Boyarsky, B.J., Werbel, W.A., Avery, R.K., Tobian, A.A.R., Massie, A.B., Segev, D.L., and Garonzik-Wang, J.M. (2021b). Immunogenicity of a single dose of SARS-CoV-2 messenger RNA vaccine in solid organ transplant recipients. JAMA *325*, 1784–1786.

Brakemeier, S., Schweiger, B., Lachmann, N., Glander, P., Schönemann, C., Diekmann, F., Neumayer, H.H., and Budde, K. (2012). Immune response to an adjuvanted influenza A H1N1 vaccine (Pandemrix(®)) in renal transplant recipients. Nephrol. Dial. Transplant. *27*, 423–428.

Broeders, N.E., Hombrouck, A., Lemy, A., Wissing, K.M., Racapé, J., Gastaldello, K., Massart, A., Van Gucht, S., Weichselbaum, L., De Mul, A., et al. (2011). Influenza A/H1N1 vaccine in patients treated by kidney transplant or dialysis: A cohort study. Clin. J. Am. Soc. Nephrol. *6*, 2573–2578.

Brouwer, P.J.M., Caniels, T.G., Straten, K. van der, Snitselaar, J.L., Aldon, Y., Bangaru, S., Torres, J.L., Okba, N.M.A., Claireaux, M., Kerster, G., et al. (2020). Potent neutralizing antibodies from COVID-19 patients define multiple targets of vulnerability. Science *369*, 643–650.

Carvalho, T., Krammer, F., and Iwasaki, A. (2021). The first 12 months of COVID-19: a timeline of immunological insights. Nat. Rev. Immunol. *21*, 245–256.

Chen, J.S., Chow, R.D., Song, E., Mao, T., Israelow, B., Kamath, K., Bozekowski, J., Haynes, W.A., Filler, R.B., Menasche, B.L., et al. (2021). High-affinity, neutralizing antibodies to SARS-CoV-2 can be made in the absence of T follicular helper cells. bioRxiv.

Chen, T., Guo, J., Yang, M., Han, C., Zhang, M., Chen, W., Liu, Q., Wang, J., and Cao, X. (2004). Cyclosporin A impairs dendritic cell migration by regulating chemokine receptor expression and inhibiting cyclooxygenase-2 expression. Blood *103*, 413–421.

Collier, D.A., De Marco, A.D., Ferreira, I.A.T.M., Meng, B., Datir, R.P., Walls, A.C., Kemp, S.A., Bassi, J., Pinto, D., Silacci-Fregni, C., et al. (2021). Sensitivity of SARS-CoV-2 B.1.1.7 to mRNA vaccine-elicited antibodies. Nature *593*, 136–141.

Cowan, M., Chon, W.J., Desai, A., Andrews, S., Bai, Y., Veguilla, V., Katz, J.M., Josephson, M.A., Wilson, P.C., Sciammas, R., et al. (2014). Impact of immunosuppression on recall immune responses to influenza vaccination in stable renal transplant recipients. Transplantation *97*, 846–853.

Crotty, S. (2019). T follicular helper cell biology: A decade of discovery and diseases. Immunity *50*, 1132–1148.

Cucchiari, D., Egri, N., Bodro, M., Herrera, S., Del Risco-Zevallos, J.D., Casals-Urquiza, J., Cofan, F., Moreno, A., Rovira, J., Banon-Maneus, E., et al. (2021). Cellular and humoral response after MRNA-1273 SARS-CoV-2 vaccine in kidney transplant recipients. Am. J. Transplant. *21*, 2727–2739.

Earle, K.A., Ambrosino, D.M., Fiore-Gartland, A., Goldblatt, D., Gilbert, P.B., Siber, G.R., Dull, P., and Plotkin, S.A. (2021). Evidence for antibody as a protective correlate for COVID-19 vaccines. Vaccine *39*, 4423–4428.

Edara, V.-V., Pinsky, B.A., Suthar, M.S., Lai, L., Davis-Gardner, M.E., Floyd, K., Flowers, M.W., Wrammert, J., Hussaini, L., Ciric, C.R., et al. (2021). Infection and vaccine-induced neutralizing-antibody responses to the SARS-CoV-2 B.1.617 Variants. N. Engl. J. Med. *385*, 664–666.

Eickenberg, S., Mickholz, E., Jung, E., Nofer, J.R., Pavenstädt, H.J., and Jacobi, A.M. (2012). Mycophenolic acid counteracts B cell proliferation and plasmablast formation in patients with systemic lupus erythematosus. Arthritis Res. Ther. *14*, R110.

Elhanan, E., Boaz, M., Schwartz, I., Schwartz, D., Chernin, G., Soetendorp, H., Gal Oz, A.G., Agbaria, A., and Weinstein, T. (2018). A randomized, controlled clinical trial to evaluate the immunogenicity of a PreS/S hepatitis B vaccine Sci-B-Vac™, as compared to Engerix B®, among vaccine naïve and vaccine non-responder dialysis patients. Clin. Exp. Nephrol. *22*, 151–158.

Espeseth, A.S., Cejas, P.J., Citron, M.P., Wang, D., DiStefano, D.J., Callahan, C., Donnell, G.O., Galli, J.D., Swoyer, R., Touch, S., et al. (2020). Modified mRNA/lipid nanoparticle-based vaccines expressing respiratory syncytial virus F protein variants are immunogenic and protective in rodent models of RSV infection. npj Vaccines *5*, 16.

Flanagan, W.M., Corthésy, B., Bram, R.J., and Crabtree, G.R. (1991). Nuclear association of a T-cell transcription factor blocked by FK-506 and cyclosporin A. Nature *352*, 803–807.

Flannery, D.D., Gouma, S., Dhudasia, M.B., Mukhopadhyay, S., Pfeifer, M.R., Woodford, E.C., Gerber, J.S., Arevalo, C.P., Bolton, M.J., Weirick, M.E., et al. (2020). SARS-CoV-2 seroprevalence among parturient women in Philadelphia. Sci. Immunol. *5*, eabd5709.

Freyn, A.W., Ramos da Silva, J., Rosado, V.C., Bliss, C.M., Pine, M., Mui, B.L., Tam, Y.K., Madden, T.D., de Souza Ferreira, L.C., Weissman, D., et al. (2020). A multi-targeting, nucleoside-modified mRNA influenza virus vaccine provides broad protection in mice. Mol. Ther. *28*, 1569–1584.

Friedrich, P., Sattler, A., Müller, K., Nienen, M., Reinke, P., and Babel, N. (2015). Comparing humoral and cellular immune response Against HBV vaccine in kidney transplant patients. Am. J. Transplant. *15*, 3157–3165.

Goel, R.R., Apostolidis, S.A., Painter, M.M., Mathew, D., Pattekar, A., Kuthuru, O., Gouma, S., Hicks, P., Meng, W., Rosenfeld, A.M., et al. (2021). Distinct antibody and memory B cell responses in SARS-CoV-2 naïve and recovered individuals following mRNA vaccination. Sci. Immunol. *6*, eabi6950.

Greaney, A.J., Loes, A.N., Gentles, L.E., Crawford, K.H.D., Starr, T.N., Malone, K.D., Chu, H.Y., and Bloom, J.D. (2021). Antibodies elicited by mRNA-1273 vaccination bind more broadly to the receptor binding domain than do those from SARS-CoV-2 infection. Sci. Transl. Med. *13*, eabi9915.

Grifoni, A., Sidney, J., Zhang, Y., Scheuermann, R.H., Peters, B., and Sette, A. (2020b). A sequence homology and bioinformatic approach can predict candidate targets for immune responses to SARS-CoV-2. Cell Host Microbe *27*, 671–680.e2.

Grifoni, A., Weiskopf, D., Ramirez, S.I., Mateus, J., Dan, J.M., Moderbacher, C.R., Rawlings, S.A., Sutherland, A., Premkumar, L., Jadi, R.S., et al. (2020a). Targets of T cell responses to SARS-CoV-2 coronavirus in humans with COVID-19 disease and unexposed individuals. Cell *181*, 1489–1501.e15.

Hall, V.G., Ferreira, V.H., Ku, T., Ierullo, M., Majchrzak-Kita, B., Chaparro, C., Selzner, N., Schiff, J., McDonald, M., Tomlinson, G., et al. (2021). Randomized trial of a third dose of mRNA-1273 vaccine in transplant recipients. N. Engl. J. Med. *385*, 1244–1246.

Havenar-Daughton, C., Lindqvist, M., Heit, A., Wu, J.E., Reiss, S.M., Kendric, K., Bélanger, S., Kasturi, S.P., Landais, E., Akondy, R.S., et al. (2016). CXCL13 is a plasma biomarker of germinal center activity. Proc. Natl. Acad. Sci. USA *113*, 2702–2707.

Heit, A., Schmitz, F., Gerdts, S., Flach, B., Moore, M.S., Perkins, J.A., Robins, H.S., Aderem, A., Spearman, P., Tomaras, G.D., et al. (2017). Vaccination establishes clonal relatives of germinal center T cells in the blood of humans. J. Exp. Med. *214*, 2139–2152.

Herati, R.S., Reuter, M.A., Dolfi, D.V., Mansfield, K.D., Aung, H., Badwan, O.Z., Kurupati, R.K., Kannan, S., Ertl, H., Schmader, K.E., et al. (2014). Circulating CXCR5+PD-1+ response predicts influenza vaccine antibody responses in young adults but not elderly adults. J. Immunol. *193*, 3528–3537.

Jackson, L.A., Anderson, E.J., Rouphael, N.G., Roberts, P.C., Makhene, M., Coler, R.N., McCullough, M.P., Chappell, J.D., Denison, M.R., Stevens, L.J., et al. (2020). An mRNA vaccine against SARS-CoV-2 — preliminary report. N. Engl. J. Med. *383*, 1920–1931.

Kamar, N., Abravanel, F., Marion, O., Couat, C., Izopet, J., and Del Bello, A.D. (2021). Three doses of an mRNA Covid-19 vaccine in solid-organ transplant recipients. N. Engl. J. Med. *385*, 661–662.

Karnell, J.L., Karnell, F.G., Stephens, G.L., Rajan, B., Morehouse, C., Li, Y., Swerdlow, B., Wilson, M., Goldbach-Mansky, R., Groves, C., et al. (2011). Mycophenolic acid differentially impacts B cell function depending on the stage of differentiation. J. Immunol. *187*, 3603–3612.

Khoury, D.S., Cromer, D., Reynaldi, A., Schlub, T.E., Wheatley, A.K., Juno, J.A., Subbarao, K., Kent, S.J., Triccas, J.A., and Davenport, M.P. (2021). Neutralizing antibody levels are highly predictive of immune protection from symptomatic SARS-CoV-2 infection. Nat. Med. *27*, 1205–1211.

Krammer, F. (2020). SARS-CoV-2 vaccines in development. Nature *586*, 516–527.

Kreer, C., Zehner, M., Weber, T., Ercanoglu, M.S., Gieselmann, L., Rohde, C., Halwe, S., Korenkov, M., Schommers, P., Vanshylla, K., et al. (2020). Longitudinal isolation of potent Near-germline SARS-CoV-2-neutralizing antibodies from COVID-19 patients. Cell *182*, 843–854.e12.

Lederer, K., Castaño, D., Atria, D.G., Oguin, T.H., Wang, S., Manzoni, T.B., Muramatsu, H., Hogan, M.J., Amanat, F., Cherubin, P., et al. (2020). SARS-CoV-2 mRNA vaccines foster potent antigen-specific germinal center responses associated with neutralizing antibody generation. Immunity *53*, 1281–1295.e5.

Lindgren, G., Ols, S., Liang, F., Thompson, E.A., Lin, A., Hellgren, F., Bahl, K., John, S., Yuzhakov, O., Hassett, K.J., et al. (2017). Induction of robust B cell responses after influenza mRNA vaccination is accompanied by circulating hemagglutinin-specific ICOS+ PD-1+ CXCR3+ T follicular helper cells. Front. Immunol. *8*, 1539.

Liu, J., Farmer, J.D., Lane, W.S., Friedman, J., Weissman, I., and Schreiber, S.L. (1991). Calcineurin is a common target of cyclophilin-cyclosporin A and FKBP-FK506 complexes. Cell *66*, 807–815.

Locci, M., Havenar-Daughton, C., Landais, E., Wu, J., Kroenke, M.A., Arlehamn, C.L., Su, L.F., Cubas, R., Davis, M.M., Sette, A., and Haddad, E.K.; International AIDS Vaccine Initiative Protocol C Principal Investigators, Poignard, P., Crotty, S (2013). Human circulating PD-1+CXCR3-CXCR5+ memory Tfh cells are highly functional and correlate with broadly neutralizing HIV antibody responses. Immunity *39*, 758–769.

Lumley, S.F., O'Donnell, D., Stoesser, N.E., Matthews, P.C., Howarth, A., Hatch, S.B., Marsden, B.D., Cox, S., James, T., Warren, F., et al. (2021). Antibody status and incidence of SARS-CoV-2 infection in health care workers. N. Engl. J. Med. *384*, 533–540.

Margine, I., Palese, P., and Krammer, F. (2013). Expression of functional recombinant hemagglutinin and neuraminidase proteins from the novel H7N9 influenza virus using the baculovirus expression system. J. Vis. Exp. *81*, e51112.

Massa, F., Cremoni, M., Gerard, A., Grabsi, H., Rogier, L., Blois, M., Hassen, N.B., Rouleau, M., Barbosa, S., Martinuzzi, E., et al. (2021). Safety and cross-variant immunogenicity of a three-dose COVID-19 mRNA vaccine regimen in kidney transplant recipients. EBioMedicine *73*, 103679.

McMahan, K., Yu, J., Mercado, N.B., Loos, C., Tostanoski, L.H., Chandrashekar, A., Liu, J., Peter, L., Atyeo, C., Zhu, A., et al. (2021). Correlates of protection against SARS-CoV-2 in rhesus macaques. Nature *590*, 630–634.

Mehling, A., Grabbe, S., Voskort, M., Schwarz, T., Luger, T.A., and Beissert, S. (2000). Mycophenolate mofetil impairs the maturation and function of murine dendritic cells. J. Immunol. *165*, 2374–2381.

Mesin, L., Ersching, J., and Victora, G.D. (2016). Germinal center B cell dynamics. Immunity *45*, 471–482.

Mohty, M. (2007). Mechanisms of action of antithymocyte globulin: T-cell depletion and beyond. Leukemia *21*, 1387–1394.

Morita, R., Schmitt, N., Bentebibel, S.E., Ranganathan, R., Bourdery, L., Zurawski, G., Foucat, E., Dullaers, M., Oh, S., Sabzghabaei, N., et al. (2011). Human blood CXCR5(+)CD4(+) T cells are counterparts of T follicular cells and contain specific subsets that differentially support antibody secretion. Immunity *34*, 108–121.

Muecksch, F., Weisblum, Y., Barnes, C.O., Schmidt, F., Schaefer-Babajew, D., Wang, Z., Lorenzi, J.C.C., Flyak, A.I., DeLaitsch, A.T., Huey-Tubman, K.E., et al. (2021). Affinity maturation of SARS-CoV-2 neutralizing antibodies confers potency, breadth, and resilience to viral escape mutations. Immunity *54*, 1853–1868.e7.

Havenar-Daughton, C., Newton, I.G., Zare, S.Y., Reiss, S.M., Schwan, B., Suh, M.J., Hasteh, F., Levi, G., and Crotty, S. (2020). Normal human lymph node T follicular helper cells and germinal center B cells accessed via fine needle aspirations. J. Immunol. Methods *479*, 112746.

Otsuka, S., Melis, N., Gaida, M.M., Dutta, D., Weigert, R., and Ashwell, J.D. (2021). Calcineurin inhibitors suppress acute graft-versus-host disease via NFAT-independent inhibition of T cell receptor signaling. J. Clin. Invest. *131*, e147683.

Painter, M.M., Mathew, D., Goel, R.R., Apostolidis, S.A., Pattekar, A., Kuthuru, O., Baxter, A.E., Herati, R.S., Oldridge, D.A., Gouma, S., et al. (2021). Rapid induction of antigen-specific CD4+ T cells is associated with coordinated humoral and cellular immunity to SARS-CoV-2 mRNA vaccination. Immunity *54*, 2133–2142.e3.

Pardi, N., Hogan, M.J., Naradikian, M.S., Parkhouse, K., Cain, D.W., Jones, L., Moody, M.A., Verkerke, H.P., Myles, A., Willis, E., et al. (2018a). Nucleoside-modified mRNA vaccines induce potent T follicular helper and germinal center B cell responses. J. Exp. Med. *215*, 1571–1588.

Pardi, N., Hogan, M.J., Pelc, R.S., Muramatsu, H., Andersen, H., DeMaso, C.R., Dowd, K.A., Sutherland, L.L., Scearce, R.M., Parks, R., et al. (2017). Zika virus protection by a single low-dose nucleoside-modified mRNA vaccination. Nature *543*, 248–251.

Pardi, N., Parkhouse, K., Kirkpatrick, E., McMahon, M., Zost, S.J., Mui, B.L., Tam, Y.K., Karikó, K., Barbosa, C.J., Madden, T.D., et al. (2018b). Nucleoside-modified mRNA immunization elicits influenza virus hemagglutinin stalk-specific antibodies. Nat. Commun. *9*, 3361.

Piemonti, L., Monti, P., Allavena, P., Sironi, M., Soldini, L., Leone, B.E., Socci, C., and Carlo, V. (1999). Glucocorticoids affect human dendritic cell differentiation and maturation. J Immunol. *162*, 6473–6481.

Planas, D., Veyer, D., Baidaliuk, A., Staropoli, I., Guivel-Benhassine, F., Rajah, M.M., Planchais, C., Porrot, F., Robillard, N., Puech, J., et al. (2021). Reduced sensitivity of SARS-CoV-2 variant Delta to antibody neutralization. Nature *596*, 276–280.

Plotkin, S.A. (2010). Correlates of protection induced by Vaccination. Clin. Vaccine Immunol. *17*, 1055–1065.

Polack, F.P., Thomas, S.J., Kitchin, N., Absalon, J., Gurtman, A., Lockhart, S., Perez, J.L., Pérez Marc, G.P., Moreira, E.D., Zerbini, C., et al. (2020). Safety and efficacy of the BNT162b2 mRNA Covid-19 vaccine. N. Engl. J. Med. *383*, 2603–2615.

Quéméneur, L., Flacher, M., Gerland, L.M., ffrench, M., Revillard, J.P., and Bonnefoy-Berard, N. (2002). Mycophenolic acid inhibits IL-2-dependent T cell proliferation, but not IL-2-dependent survival and sensitization to apoptosis. J. Immunol. *169*, 2747–2755.

Rencher, A.C. (2002). Methods of multivariate analysis, 2nd edition (Wiley-Interscience).

Richner, J.M., Himansu, S., Dowd, K.A., Butler, S.L., Salazar, V., Fox, J.M., Julander, J.G., Tang, W.W., Shresta, S., Pierson, T.C., et al. (2017). Modified mRNA vaccines protect against Zika virus infection. Cell *169*, 176.

Rincon-Arevalo, H., Choi, M., Stefanski, A.L., Halleck, F., Weber, U., Szelinski, F., Jahrsdörfer, B., Schrezenmeier, H., Ludwig, C., Sattler, A., et al. (2021). Impaired humoral immunity to SARS-CoV-2 BNT162b2 vaccine in kidney transplant recipients and dialysis patients. Sci. Immunol. *6*, eabj1031.

Rogers, T.F., Zhao, F., Huang, D., Beutler, N., Burns, A., He, W.T., Limbo, O., Smith, C., Song, G., Woehl, J., et al. (2020). Isolation of potent SARS-CoV-2 neutralizing antibodies and protection from disease in a small animal model. Science *369*, 956–963.

Sahin, U., Muik, A., Derhovanessian, E., Vogler, I., Kranz, L.M., Vormehr, M., Baum, A., Pascal, K., Quandt, J., Maurus, D., et al. (2020). COVID-19 vaccine BNT162b1 elicits human antibody and TH1 T cell responses. Nature *586*, 594–599.

Sallusto, F., Lanzavecchia, A., Araki, K., and Ahmed, R. (2010). From vaccines to memory and back. Immunity *33*, 451–463.

Sattler, A., Schrezenmeier, E., Weber, U.A., Potekhin, A., Bachmann, F., Straub-Hohenbleicher, H., Budde, K., Storz, E., Proß, V., Bergmann, Y., et al. (2021). Impaired humoral and cellular immunity after SARS-CoV-2 BNT162b2 (Tozinameran) prime-boost vaccination in kidney transplant recipients. J. Clin. Invest. *131*, e150175.

Schultheiß, C., Paschold, L., Simnica, D., Mohme, M., Willscher, E., Wenserski, L. von, Scholz, R., Wieters, I., Dahlke, C., Tolosa, E., et al. (2020). Next-generation sequencing of T and B cell receptor repertoires from COVID-19 patients showed signatures associated with severity of disease. Immunity *53*, 442–455.e4.

Seydoux, E., Homad, L.J., Maccamy, A.J., Parks, K.R., Hurlburt, N.K., Jennewein, M.F., Akins, N.R., Stuart, A.B., Wan, Y.H., Feng, J., et al. (2020). Analysis of a SARS-CoV-2-infected individual reveals development of potent neutralizing antibodies with limited somatic mutation. Immunity *53*, 98–105.e5.

Sprent, P. (2019). Data driven statistical methods (Routledge).

Stadlbauer, D., Amanat, F., Chromikova, V., Jiang, K., Strohmeier, S., Arunkumar, G.A., Tan, J., Bhavsar, D., Capuano, C., Kirkpatrick, E., et al. (2020). SARS-CoV-2 seroconversion in humans: A detailed protocol for a serological assay, antigen production, and test setup. Curr. Protoc. Microbiol. *57*, e100.

Stamatatos, L., Czartoski, J., Wan, Y.H., Homad, L.J., Rubin, V., Glantz, H., Neradilek, M., Seydoux, E., Jennewein, M.F., Maccamy, A.J., et al. (2021). mRNA vaccination boosts cross-variant neutralizing antibodies elicited by SARS-CoV-2 infection. Science *372*, 1413–1418.

Stumpf, J., Siepmann, T., Lindner, T., Karger, C., Schwöbel, J., Anders, L., Faulhaber-Walter, R., Schewe, J., Martin, H., Schirutschke, H., et al. (2021). Humoral and cellular immunity to SARS-CoV-2 vaccination in renal transplant versus dialysis patients: A prospective, multicenter observational study using mRNA-1273 or BNT162b2 mRNA vaccine. Lancet Reg Health Eur. *30*, 100178.

Tai, W., Zhang, X., Drelich, A., Shi, J., Hsu, J.C., Luchsinger, L., Hillyer, C.D., Tseng, C.-T.K., Jiang, S., and Du, L. (2020). A novel receptor-binding domain (RBD)-based mRNA vaccine against SARS-CoV-2. Cell Res *30*, 932–935.

Taves, M.D., and Ashwell, J.D. (2021). Glucocorticoids in T cell development, differentiation and function. Nat. Rev. Immunol. *21*, 233–243.

Trifari, S., Kaplan, C.D., Tran, E.H., Crellin, N.K., and Spits, H. (2009). Identification of a human helper T cell population that has abundant production of interleukin 22 and is distinct from T(H)-17, T(H)1 and T(H)2 cells. Nat. Immunol. *10*, 864–871.

Turner, J.S., O'Halloran, J.A., Kalaidina, E., Kim, W., Schmitz, A.J., Zhou, J.Q., Lei, T., Thapa, M., Chen, R.E., Case, J.B., et al. (2021). SARS-CoV-2 mRNA

vaccines induce persistent human germinal centre responses. Nature *596*, 109–113.

Turner, J.S., Zhou, J.Q., Han, J., Schmitz, A.J., Rizk, A.A., Alsoussi, W.B., Lei, T., Amor, M., McIntire, K.M., Meade, P., et al. (2020). Human germinal centres engage memory and naive B cells after influenza vaccination. Nature *586*, 127–132.

Ueno, H. (2016). Human circulating T follicular helper cell subsets in health and disease. J. Clin. Immunol. *36* (*Supplement 1*), 34–39.

Vaeth, M., Maus, M., Klein-Hessling, S., Freinkman, E., Yang, J., Eckstein, M., Cameron, S., Turvey, S.E., Serfling, E., Berberich-Siebelt, F., et al. (2017). Store-operated Ca2+ entry controls clonal expansion of T cells through metabolic reprogramming. Immunity *47*, 664–679.e6.

Vella, L.A., Buggert, M., Manne, S., Herati, R.S., Sayin, I., Kuri-Cervantes, L., Bukh Brody, I.B., O'Boyle, K.C., Kaprielian, H., Giles, J.R., et al. (2019). T follicular helper cells in human efferent lymph retain lymphoid characteristics. J. Clin. Invest. *129*, 3185–3200.

Vinuesa, C.G., Linterman, M.A., Yu, D., and MacLennan, I.C.M. (2016). Follicular helper T cells. Annu. Rev. Immunol. *34*, 335–368.

Vogel, A.B., Kanevsky, I., Che, Y., Swanson, K.A., Muik, A., Vormehr, M., Kranz, L.M., Walzer, K.C., Hein, S., Güler, A., et al. (2021). BNT162b vaccines protect rhesus macaques from SARS-CoV-2. Nature *592*, 283–289.

Wallin, E.F., Hill, D.L., Linterman, M.A., and Wood, K.J. (2018). The calcineurin inhibitor tacrolimus specifically suppresses human T follicular helper cells. Front. Immunol. *9*, 1184.

Walsh, E.E., Jr., Frenck, R.W., Falsey, A.R., Kitchin, N., Absalon, J., Gurtman, A., Lockhart, S., Neuzil, K., Mulligan, M.J., Bailey, R., et al. (2020). Safety and immunogenicity of two RNA-based Covid-19 vaccine candidates. N. Engl. J. Med. *383*, 2439–2450.

Wang, Z., Muecksch, F., Schaefer-Babajew, D., Finkin, S., Viant, C., Gaebler, C., Hoffmann, H.H., Barnes, C.O., Cipolla, M., Ramos, V., et al. (2021b). Naturally enhanced neutralizing breadth against SARS-CoV-2 one year after infection. Nature *595*, 426–431.

Wang, Z., Schmidt, F., Weisblum, Y., Muecksch, F., Barnes, C.O., Finkin, S., Schaefer-Babajew, D., Cipolla, M., Gaebler, C., Lieberman, J.A., et al. (2021a). mRNA vaccine-elicited antibodies to SARS-CoV-2 and circulating variants. Nature *592*, 616–622.

Widge, A.T., Rouphael, N.G., Jackson, L.A., Anderson, E.J., Roberts, P.C., Makhene, M., Chappell, J.D., Denison, M.R., Stevens, L.J., Pruijssers, A.J., et al. (2021). Durability of responses after SARS-CoV-2 mRNA-1273 vaccination. N. Engl. J. Med. *384*, 80–82.

Wrapp, D., Wang, N., Corbett, K.S., Goldsmith, J.A., Hsieh, C.L., Abiona, O., Graham, B.S., and McLellan, J.S. (2020). Cryo-EM structure of the 2019-nCoV spike in the prefusion conformation. Science *367*, 1260–1263.

Zost, S.J., Gilchuk, P., Case, J.B., Binshtein, E., Chen, R.E., Nkolola, J.P., Schäfer, A., Reidy, J.X., Trivette, A., Nargi, R.S., et al. (2020). Potently neutralizing and protective human antibodies against SARS-CoV-2. Nature *584*, 443–449.

STAR★METHODS

KEY RESOURCES TABLE

REAGENT or RESOURCE	SOURCE	IDENTIFIER
Antibodies		
anti-human CXCR5 BUV395	BD Biosciences	Cat#740266; RRID: AB_2740008
anti-human CCR4 PE-CF594	BD Biosciences	Cat#565391; RRID: AB_2739215
anti-human CCR6 BV480	BD Biosciences	Cat#566130; RRID: AB_2739529
anti-human CXCR3 BV510	Biolegend	Cat#353726; RRID: AB_2563642
anti-human IgM BUV496	BD Biosciences	Cat#750366; RRID: AB_2874541
anti-human CD4 BUV563	BD Biosciences	Cat#612912; RRID: AB_2739451
anti-human CD11c BUV661	BD Biosciences	Cat#612967, RRID: AB_2870241
anti-human IgD BUV737	BD Biosciences	Cat#612798; RRID: AB_2738894
anti-human CD45RA BUV805	BD Biosciences	Cat#742020; RRID: AB_2871317
anti-human CD138 BV605	Biolegend	Cat#356520; RRID: AB_2562862
anti-human ICOS BV650	Biolegend	Cat#313550; RRID: AB_2749929
anti-human CD20 BV750	BD Biosciences	Cat#747062; RRID: AB_2871819
anti-human CD38 BV785	Biolegend	Cat#303530; RRID: AB_2565893
anti-human CD8α PerCP-eFluor710	Invitrogen	Cat#46-0086-42; RRID: AB_2848331
anti-human CD27 PE-Cy5	Invitrogen	Cat#15-0279-42; RRID: AB_10717249
anti-human CD19 PE-Cy5.5	Invitrogen	Cat#35-0198-42; RRID: AB_11218903
anti-human CD11b Alexa Fluor 700	Biolegend	Cat#301356; RRID: AB_2750075
anti-human PD-1 PE-Cy7	Biolegend	Cat#329918; RRID: AB_2159324
anti-human/mouse BCL6 Alexa Fluor 647	BD Biosciences	Cat#561525; RRID: AB_10898007
anti-human CD4 BUV395	BD Biosciences	Cat#563550; RRID: AB_2738273
anti-human CD8 BUV496	BD Biosciences	Cat#612942, RRID: AB_2870223
anti-human CD45RA BUV615	BD Biosciences	Cat#751555; RRID: AB_2875550
anti-human CD27 BUV737	BD Biosciences	Cat#612829; RRID: AB_2870151
anti-human CD8 BUV805	BD Biosciences	Cat#612896; RRID: AB_2870184
anti-human CXCR3 BV421	Biolegend	Cat#353716; RRID: AB_2561448
anti-human CCR7 BV650	Biolegend	Cat#353234; RRID: AB_2563867
anti-human CD69 BV605	Biolegend	Cat#310938; RRID: AB_2562307
anti-human CD40L BV711	Biolegend	Cat#310838; RRID: AB_2563845
anti-human CD107a BV785	Biolegend	Cat#328644; RRID: AB_2565968
anti-human IFNγ FITC	Biolegend	Cat#502515; RRID: AB_493029
anti-human CD200 PE	Biolegend	Cat#399804; RRID: AB_2861016
anti-human OX40 PE-Cy7	Biolegend	Cat#350012; RRID: AB_10901161
anti-human 4-1BB Alexa Fluor 647	Biolegend	Cat#309810; RRID: AB_830672
anti-human CXCR5 APC-R700	BD Biosciences	Cat#565191; RRID: AB_2739103
anti-human CCR6 APC-Cy7	Biolegend	Cat#353432; RRID: AB_2566274
anti-human CD40, purified	Miltenyi Biotec	Cat#130-094-133; RRID: AB_10839704
anti-human CD28/CD49d, purified	BD Biosciences	Cat#347690; RRID: AB_647457
Goat anti-human IgG-HRP	Jackson ImmunoResearch	Cat#109-036-098; RRID: AB_2337596
Goat anti-human IgM-HRP	Southern Biotech	Cat#2020-05; RRID: AB_2795603
Goat anti-human IgA-HRP	Southern Biotech	Cat#2050-05; RRID: AB_2687526
Bacterial and virus strains		
SARS-CoV-2 VSV pseudotypes	Generated for this paper	N/A

(*Continued on next page*)

Continued

REAGENT or RESOURCE	SOURCE	IDENTIFIER
Biological samples		
Human FNA	Perelman Center for Advanced Medicine	N/A
Human PBMCs	Perelman Center for Advanced Medicine	N/A
Human lymph nodes	National Disease Resource Interchange	N/A
Human pediatric tonsils	Children's Hospital of Philadelphia	N/A
Chemicals, peptides, and recombinant proteins		
Fixable viability dye eFluor 780	Invitrogen	Cat#65086518
Recombinant RBD	Florian Krammer	Amanat et al., 2020
Recombinant Spike-Biotin	R&D Systems	Cat#BT10549-050
Recombinant PR8 HA	Norbert Pardi	N/A
Streptavidin BV421	Biolegend	Cat#405225
Streptavidin Alexa Fluor 488	Biolegend	Cat#405235
Streptavidin Alexa Fluor 647	Biolegend	Cat#405237
EZ-Link Micro Sulfo-NHS-LC-Biotinylation Kit	Thermo Fisher Scientific	Cat#21935
FoxP3 / Transcription Factor Staining Buffer Set	Thermo Fisher Scientific	Cat#00-5523-00
Ghost Dye Violet 510	Tonbo	Cat#13-0870-T500
GolgiStop (Containing Monensin)	BD Biosciences	Cat#51-2092K7
Human TruStain FcX™ (Fc Receptor Blocking Solution)	Biolegend	Cat#422302
Brilliant Stain Buffer	BD Biosciences	Cat#563794
ACK Lysing Buffer	Gibco	Cat#A10492-01
Ficoll-Paque	Cytvia	Cat#17-440-02
OC43 FL spike protein	Sino Biological	Cat#40607-V08B
SARS-CoV-2 spike protein	Expressed for this paper	N/A
SARS-CoV-2 RBD protein	Expressed for this paper	N/A
Critical commercial assays		
Human anti-measles IgG ELISA kit	Alpha Diagnostic International	Cat#530-100-HMG
Human anti-rubella IgG ELISA kit	Phoenix Biotech	Cat#EK-310-81
Human anti-mumps IgG ELISA kit	Calbiotech	Cat#MP060G
Human anti-tetanus toxoid IgG ELISA kit	VaccZyme	Cat#MK010.U
Experimental models: Cell lines		
293F	Thermo Fisher	Cat#R79007
293T	ATCC	Cat#CRL-3216; RRID: CVCL_0063
VeroE6/TMPRSS	Stefan Pohlman	Anderson et al., 2021b.
Recombinant DNA		
Plasmid: pCAGGS SARS-CoV-2 spike	Florian Krammer	Amanat et al. (2020)
Plasmid: pCAGGS SARS-CoV-2 RBD	Florian Krammer	Amanat et al. (2020)
Plasmid: pCG1 SARS-CoV-2 D614G delta18	Bates Lab	N/A
Plasmid: pCG1 SARS-CoV-2 S B.1.351 delta 18	Bates Lab	N/A
Software and algorithms		
Graphpad Prism v9	Graphpad	RRID:SCR_002798
FlowJo v10	FlowJo LLC	RRID:SCR_008520
Cytobank Premium	Beckman Coulter	RRID:SCR_014043
R version 4.0.3		N/A

RESOURCE AVAILABILITY

Lead contact

Further information and requests for resources and reagents should be directed to and will be fulfilled by the lead contact, Michela Locci (michela.locci@pennmedicine.upenn.edu).

Materials availability

All unique reagents generated in this study will be available from the lead contact upon reasonable request.

Data and code availability

All raw data reported in this paper will be shared by the lead contact upon request.

This paper does not report original code.

Any additional information required to reanalyze the data reported in this paper is available from the lead contact upon request.

EXPERIMENTAL MODEL AND SUBJECT DETAILS

Study design and human samples

The prospective cohort study included 15 healthy adults and 15 kidney transplant recipients at the Hospital of the University of Pennsylvania across both the lymph node and blood samples analyses (Table S1). The healthy donor cohort ranged in age from 23 to 76 years old and was composed of six males and nine females. The KTX recipient cohort ranged in age from 28 to 70 years old and was composed of nine males and six females. All participants received two doses of either BNT162b2 or mRNA-1273 vaccines, according to the recommended 3- and 4-week interval, respectively. Most participants received the first and second immunizations in the same arm. Written informed consent for participation was obtained according to the Declaration of Helsinki and protocols were approved by the Institutional Review Board of the University of Pennsylvania. Lymph node samples were obtained by ultrasound-guided fine needle aspiration at day 12 (+/- 3 days) after primary immunization and at day 10 (+/- 2 days) after a second immunization. Blood samples were obtained at baseline prior to vaccination (visit 1, V1), day 12 (+/- 3 days) following primary immunization (visit 2, V2), and day 10 (+/- 2 days) following a second immunization (visit 3, V3). In four kidney transplant recipients, blood and FNA samples were also obtained prior to visit 4(V4) and at day 8 (+/- 2 days) (visit 5, V5) following a 3rd vaccine dose.

Lymph nodes and pediatric tonsils were obtained from the National Disease Resource Interchange (NDRI), and the Children's Hospital of Philadelphia (CHOP), respectively.

METHOD DETAILS

Ultrasound guided fine needle aspiration

All fine needle aspirations (FNA) were performed by board-certified radiologists, similar to what previously described (Havenar-Daughton et al., 2020). Briefly, a Philips EPIQ ELITE or PHILIPS IU222 ultrasound instrument was used to visualize axillary draining lymph nodes. The area around the lymph node was anesthetized using 2-6mL of 0.9% buffered lidocaine solution. A 25-gauge needle was inserted into the cortex and moved back-and-forth several times, sample was aspirated and ejected into cold RPMI media containing 10% FBS. A total of five such passes were performed. In all participants, FNAs were performed on the side of vaccination (ipsilateral). In 4 participants, additional FNA was performed on the contralateral side after the second immunization.

Blood processing

Isolation of serum

Blood was collected in serum separator tubes (Becton Dickinson) which were spun at 935g for 15 minutes. Serum was collected, aliquoted, and frozen at -80°C for subsequent use.

Isolation of peripheral blood mononuclear cells (PBMCs)

PBMCs were isolated from blood collected in sodium heparin vacutainer tubes (Becton Dickinson). Briefly, whole blood was first spun at 935g for 15min. The plasma was carefully collected, aliquoted and stored at -80°C. The buffy layer and red cell sediment were diluted with an equal volume of RPMI with 5% FBS (RPMI-5) and gently layered over 15mL of Ficoll-Paque Plus (Cytiva) in a 50mL SepMate tube (STEMCELL Technologies). The sample was centrifuged at 1200g for 10 minutes. The PBMC were transferred into a new 50mL conical tube, centrifuged, decanted, and washed twice with RPMI-5 before flow cytometry staining or cryopreservation in FBS with 10% dimethyl sulfoxide.

Production of fluorescently labeled proteins

Labeling of SARS-CoV-2 full-length spike protein

Full-length, biotinylated spike protein was purchased from R&D Systems. Streptavidin-conjugated BV421 (Biolegend) was then added at a 6:1 molar ratio (biotinylated-protein to streptavidin-conjugate) on ice for 1 hour.

Labeling of HA and SARS-CoV-2 RBD

Recombinant HA and RBD was produced as previously described (Amanat et al., 2020; Margine et al., 2013; Stadlbauer et al., 2020). To create fluorescently labeled RBD tetramers, RBD was biotinylated using the EZ-Link Micro Sulfo-NHS-Biotinylation Kit (ThermoFisher). Streptavidin-conjugated PE was then added at a 6:1 molar ratio (biotinylated-protein to streptavidin-conjugate). Specifically, after the volume of fluorochrome needed to achieve a 6:1 molar ratio was determined, the total volume of fluorochrome

was split into 10 subaliquots. These subaliquots were then added, on ice, to the biotinylated protein and mixed by pipetting every 10 minutes (for a total of 10 additions).

Flow cytometry

Staining was performed on freshly isolated FNA and PBMC samples or cryopreserved control LN and tonsil samples. Up to 10^6 cells were incubated with a cocktail of chemokine receptor antibodies in FACS buffer (PBS containing 2% FBS and 1mM EDTA) for 10 minutes at 37°C. All remaining steps were carried out at 4°C. Without washing, a 2x cocktail of all other surface antibodies diluted in Brilliant Violet Staining Buffer (BD Biosciences) was added directly and incubated for 1 hour. Cells were washed with FACS buffer, fixed and permeabilized with FoxP3 Fixation/Permeabilization Buffer (eBioSciences) according to manufacturer's instructions for 1 hour, and incubated with anti-BCL6 mAb (BD Biosciences) for 30 minutes. The 23-color panel used in this study is described in Table S3. Samples were washed, resuspended in FACS buffer and immediately acquired on an Aurora using SpectroFlow v2.2 (Cytek). Data was analyzed using FlowJo v.10 (Treestar). Frequency values for individual cell populations are provided in Table S4.

viSNE analysis

viSNE analysis was performed on Cytobank (https://cytobank.org).

Class-switched B cell analysis

Cells were defined as live, $CD8^-$, $CD4^-$, $CD19^+$, IgD^- IgM^-. viSNE analysis was performed using 3200 cells from n = 3 donors per cohort with 5000 iterations, a perplexity of 60 and a theta of 0.5. The following markers and/or probes were used to generate viSNE projections: CXCR5, CD11b, CD11c, CD20, CD27, CD38, BCL6, CCR4, CCR6, CXCR3, CD138, ICOS, PD-1, RBD Probe, Full S Probe, HA Probe.

$CXCR5^+$ CD4 T cell analysis

Cells were defined as live, $CD8^-$, $CD19^-$, $CD4^+$, $CD45RA^-$ $CXCR5^+$. Analysis was performed using 2730 cells from n = 3 donors per cohort with 5000 iterations, a perplexity of 100 and a theta of 0.5. The following markers and/or probes were used to generate viSNE projections: PD-1, BCL6, CCR4, CCR6, CXCR3, CD11b, CD11c, CD20, CD27, CD38, ICOS.

Activation-induced marker expression assay

The activation-induced marker (AIM) assay was performed as previously described (Painter et al., 2021). Briefly, after thawing and counting, cells were resuspended in fresh RPMI with 10% FBS (R10) to a final density of $10x10^6$ cells/mL, and $2x10^6$ cells in 200μL were plated in duplicate wells in 96-well round-bottom plates. After resting overnight, CD40 blocking antibody was added to both duplicate wells for 15 minutes prior to stimulation. One of the duplicate wells was then stimulated for 24 hours with costimulation (anti-human CD28/CD49d, BD Biosciences) and the Spike peptide megapool at a final concentration of 1 mg/mL, while the other well was treated with costimulation alone as a paired unstimulated sample. The CD4-S peptide megapool consists of 253 overlapping 15-mer peptides spanning the entire sequence of the Spike protein and was prepared as previously described (Grifoni et al., 2020b, 2020a). The remainder of the AIM assay was performed and samples were collected and analyzed as previously described (Painter et al., 2021). The flow cytometry panel used for the the detection of AIM^+ cell populations is described in Table S5.

AIM^+ cells were identified from non-naïve or total T cell populations where indicated. All data from AIM expression assays were background-subtracted using paired unstimulated control samples. For T cell subsets, the AIM^+ background frequency of $CD45RA^-$ T cells was subtracted independently for each subset. AIM^+ CD4 T cells were defined by dual-expression of CD200 and CD40L. AIM^+ CD8 T cells were defined by either expression of 41BB and IFNγ or a boolean analysis identifying cells expressing at least three of five markers: CD200, CD40L, 41BB, CD107a, and intracellular IFNγ.

AIM assay data in Figures 6D and 6E, S6C, S6D, S6G, and S6H were visualized using RStudio. Boxplots represent median with interquartile range. Source code and data files are available upon request from the authors.

Enzyme-linked immunosorbent assay

SARS-CoV-2 and OC43 ELISAs

ELISAs were performed using a previously described protocol (Anderson et al., 2021a, 2021b; Flannery et al., 2020). Plasmids expressing the receptor binding domain (RBD) of the SARS-CoV-2 spike protein and the full-length (FL) spike protein were provided by F. Krammer (Mt. Sinai). SARS-CoV-2 RBD and FL proteins were produced in 293F cells and purified using nickel–nitrilotriacetic acid (Ni-NTA) resin (Qiagen). The supernatant was incubated with Ni-NTA resin at room temperature for 2 hours before collection using gravity flow columns and protein elution. After buffer exchange into phosphate-buffered saline (PBS), the purified protein was aliquoted and stored at −80°C. OC43 FL spike protein was purchased from Sino Biological (Cat. 40607-V08B). ELISA plates (Immulon 4 HBX, Thermo Fisher Scientific) were coated with PBS (50 μl per well) or a recombinant SARS-CoV-2 RBD or FL proteins (2 μg/ml), or a recombinant OC43 FL protein (1.5 μg/mL) diluted in PBS and stored overnight at 4°C. ELISA plates were washed three times with PBS containing 0.1% Tween 20 (PBS-T) and blocked for 1 hour with PBS-T containing 3% nonfat milk powder. Serum samples that had been previously heat-inactivated (56°C for 1 hour) were serially diluted four-fold in 96-well round-bottom plates in PBS-T supplemented with 1% nonfat milk powder (dilution buffer), starting at a 1:50 dilution. ELISA plates were then washed three times with PBS-T. 50 μl of serum dilution was added to each well and incubated at room temperature for 2 hours. Plates were then

washed again with PBS-T three times and 50 μl of horseradish peroxidase (HRP)–labeled goat anti-human IgG (1:5000; Jackson ImmunoResearch Laboratories), goat anti-human IgM HRP (1:1000, Southern Biotech), or goat anti-human IgA (1:5000; Southern Biotech) secondary antibodies was added. After 1-hour incubation at room temperature, plates were washed three times with PBS-T, 50 μl of SureBlue 3,3′,5,5′-tetramethylbenzidine substrate (KPL) was added to each well, and 25 μl of 250 mM hydrochloric acid was added to each well to stop the reaction five minutes later. Plates were read at an optical density (OD) of 450 nm using the SpectraMax 190 microplate reader (Molecular Devices). All incubation and washing steps were performed using a plate mixer. For analyses, OD values from the plates coated with PBS were subtracted from the OD values from plates coated with recombinant protein, to control for background ELISA antibody binding. Each plate contained a dilution series of the IgG monoclonal antibody CR3022, (for SARS-CoV-2 ELISAs) or serially diluted pooled serum (for OC43 ELISAs) to control for variability between assays. Serum antibody concentrations were reported as arbitrary units relative to the CR3022 monoclonal antibody.

Tetanus toxoid, measles, mumps, and rubella ELISAs

Single-timepoint measurements of IgG against tetanus toxoid, mumps, measles, and rubella, was performed on plasma samples from all subjects who participated in the FNA or blood study with the exception of 1 HD (sample unavailable). If available, baseline samples were used; In 2/14 HD and 7/13 KTX subjects, post vaccination samples were used. For tetanus toxoid (VaccZyme), measles (Alpha Diagnostics), mumps (Calbiotech), and rubella (Phoenix Biotech) ELISAs, the manufacturer's protocol was followed. In brief, samples were diluted 1:20 (mumps), 1:40 (rubella) or 1:100 (measles and tetanus toxoid), in the appropriate diluent and 100 μl of sample or standard was added to the appropriate wells of a pre-coated 96-well plate. Plates were incubated at room temperature for 20 (mumps), 30 (rubella and tetanus toxoid) or 60 (measles) minutes then plates were washed 3-5X in the appropriate wash buffer. 100 μl of secondary antibody was added to all wells and incubated at room temperature for 20 (mumps) or 30 (mumps, rubella, and tetanus toxoid) minutes before being washed 3-5X. 100 μl of substrate was then added to all wells and incubated at room temperature for 15 (rubella) or 20 (measles, mumps, and tetanus toxoid) minutes before 100 μl of stop solution was added. Plates were read at 450nM on a Molecular Devices EMax Plus plate reader. A second order polynomial regression was fit to the data in excel v16.55. All samples were run as technical duplicates and the values were averaged prior to plotting.

Pseudovirus neutralization assay

Production of VSV pseudotypes with SARS-CoV-2 S

293T cells plated 24 hours previously at 5×10^6 cells per 10 cm dish were transfected using calcium phosphate with 35 μg of pCG1 SARS-CoV-2 S D614G delta18 or pCG1 SARS-CoV-2 S B.1.351 delta 18 expression plasmid encoding a codon optimized SARS-CoV2 S gene with an 18 residue truncation in the cytoplasmic tail. Twelve hours post transfection the cells were fed with fresh media containing 5mM sodium butyrate to increase expression of the transfected DNA. Thirty hours after transfection, the SARS-CoV-2 spike expressing cells were infected for 2-4 hours with VSV-G pseudotyped VSVΔG-RFP at a MOI of ~1-3. After infection, the cells were washed twice with media to remove unbound virus. Media containing the VSVΔG-RFP SARS-CoV-2 pseudotypes was harvested 28-30 hours after infection and clarified by centrifugation twice at 6000g then aliquoted and stored at -80 °C until used for antibody neutralization analysis.

Antibody neutralization assay using VSVΔG-RFP SARS-CoV-2

All sera were heat-inactivated for 30 minutes at 55 °C prior to use in neutralization assay. Vero E6 cells stably expressing TMPRSS2 were seeded in 100 μl at $2.5x10^4$ cells/well in a 96 well collagen coated plate. The next day, 2-fold serially diluted serum samples were mixed with VSVΔG-RFP SARS-CoV-2 pseudotyped virus (100-300 focus forming units/well) and incubated for 1hr at 37 °C. Also included in this mixture to neutralize any potential VSV-G carryover virus was 1E9F9, a mouse anti-VSV Indiana G, at a concentration of 600 ng/ml (Absolute Antibody). The serum-virus mixture was then used to replace the media on VeroE6 TMPRSS2 cells. 22 hours post infection, the cells were washed and fixed with 4% paraformaldehyde before visualization on an S6 FluoroSpot Analyzer (CTL, Shaker Heights OH). Individual infected foci were enumerated and the values compared with control wells without antibody. The focus reduction neutralization titer 50% ($FRNT_{50}$) was measured as the greatest serum dilution at which focus count was reduced by at least 50% relative to control cells that were infected with pseudotyped virus in the absence of human serum. $FRNT_{50}$ titers for each sample were measured in at least two technical replicates and were reported for each sample as the geometric mean.

QUANTIFICATION AND STATISTICAL ANALYSIS

GraphPad Prism software version 9 or RStudio were used for generating all plots and correlation images presented in this work. All statistical analysis was performed in R version 4.0.3, using the following packages: ggplot2, Semblance, multicross, crossmatchtest, dplyr, randtests, ggpubr, and merTools. The following functions were used —runs.test(), wilcox.test(), crossmatchtest() and mcm() per the original statistician developer's instructions. The departure of the data from a normal/Gaussian distribution was confirmed by the Shapiro-Wilk test and consequently, nonparametric, distribution-free tests were used for all comparisons throughout this work. Single comparisons between variables were performed using the two-tailed Mann-Whitney U test with continuity correction when the number of data points in each group was greater than seven. Else, the Wald–Wolfowitz runs test was employed to afford greater sensitivity to the analysis (Sprent, 2019). Univariate correlations involving continuous and categorical data were performed

using the rank-based Spearman correlation analysis. The reported p-values are corrected for multiple hypothesis testing using the Benjamini-Hochberg procedure (Benjamini and Hochberg, 1995). Multivariate regression analyses were used to estimate the association between a given dependent variable and a set of predictors or independent variables. The null hypothesis was calculated as follows: in $X \sim \beta_0 + \beta_1 Y_1 + \beta_2 Y_2$, H_0: $\beta_1 = \beta_2 = 0$, where β_0 = intercept and $\beta_1, \ldots, \beta_n$ = regression coefficients. The multiple correlation coefficient was computed in each multiple regression analysis model to estimate the proportion of variance of the dependent variable explained by the independent variables, and its significance was computed using the F statistic (Rencher, 2002).

Statistical significance for all comparisons was set at the critical values of $p < 0.05$ (*), $p < 0.01$ (**), $p < 0.001$ (***), and $p < 0.0001$ (****).

Supplemental figures

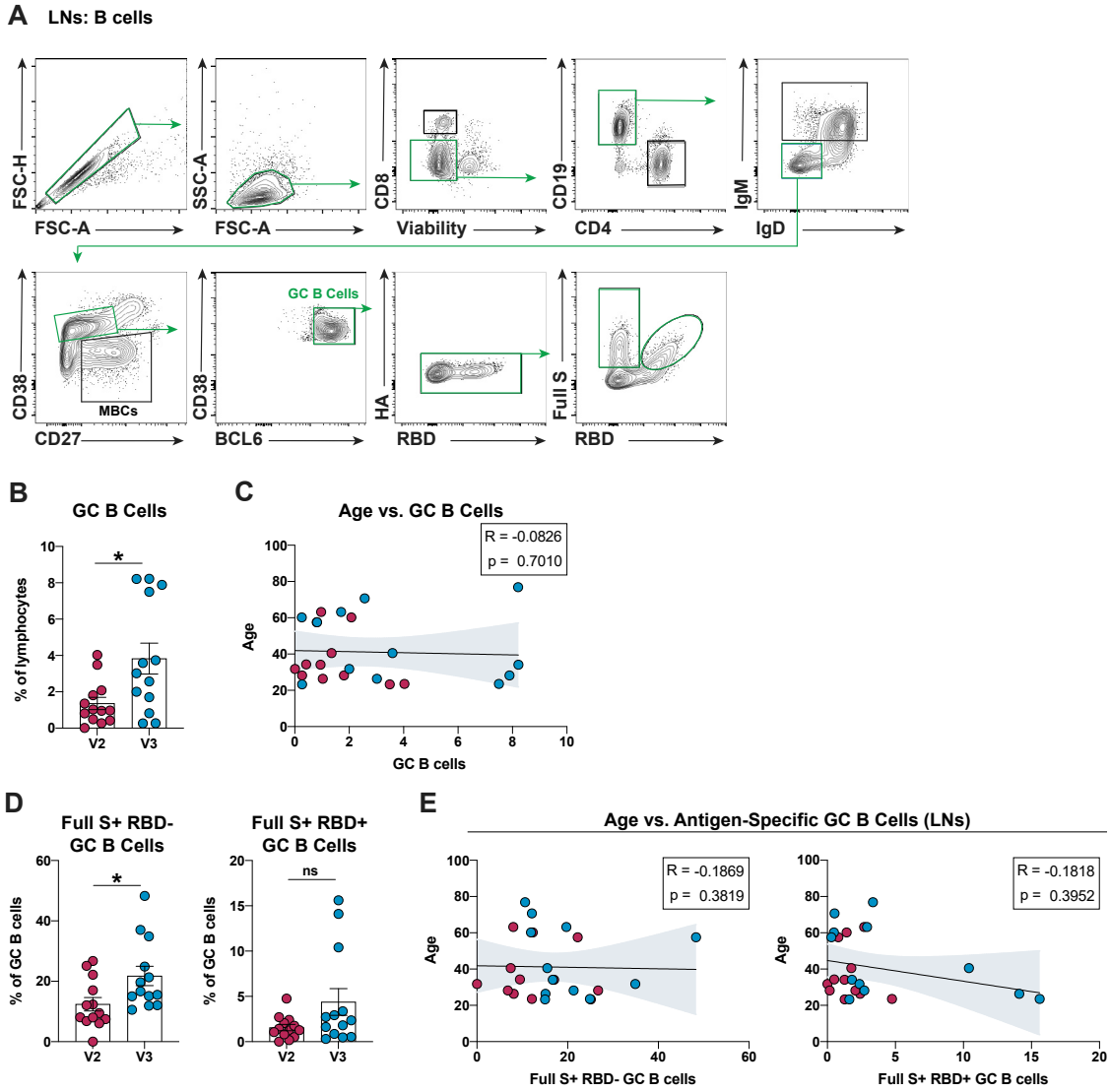

Figure S1. GC B cell responses to SARS-CoV-2 mRNA vaccines are detectable in vaccine-draining LNs of HDs, related to Figure 1

(A) Representative flow cytometry gating strategy for defining GC B cells ($CD19^+CD4^-CD8^-IgM^-IgD^-CD38^+CD27^{lo/int}BCL6^+$), SARS-CoV-2-specific GC B cells ($CD19^+CD4^-CD8^-IgM^-IgD^-CD38^+CD27^{lo/int}BCL6^+HA^-S^+RBD^{+/-}$), and class-switched MBCs ($CD19^+CD4^-CD8^-IgM^-IgD^-CD38^-CD27^+$).

(B) Quantification of GC B cells from draining LNs of HDs. Unpaired changes between V2 and V3 are shown.

(C) Spearman correlation between HD age (years) and GC B cells (displayed as a percentage of lymphocytes) at V2 (red) and V3 (blue).

(D) Unpaired analysis of Full S^+ RBD^- and Full S^+ RBD^+ GC B cells from HD draining LNs.

(E) Spearman correlation between HD age (years) and SARS-CoV-2-specific GC B cells (displayed as a percentage of GC B cells) at V2 (red) and V3 (blue).

In (B–E), n = 11–13. In (B and D), data are graphed as mean ± SEM. Statistical analysis: in (B and D), an unpaired Mann-Whitney U test with continuity correction was performed. In (C) and (E), correlations were determined using the Spearman's rho with a 95% confidence interval. * $p \leq 0.05$. See also Table S4.

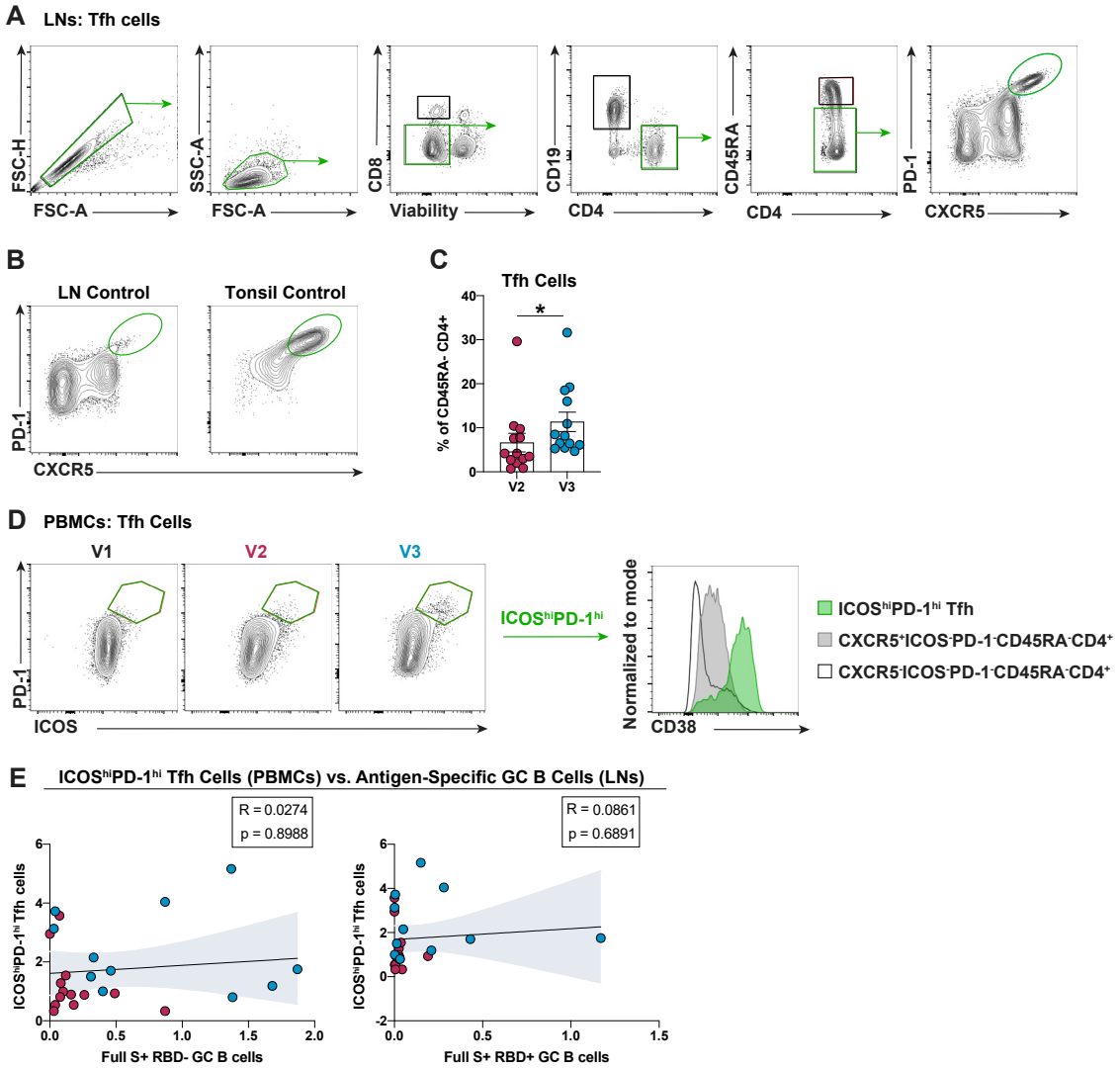

Figure S2. Tfh cell frequencies increase following immunization with SARS-CoV-2 mRNA vaccines, related to Figure 2

(A) Representative gating strategy for defining Tfh cells ($CD4^+CD8^-CD19^-CD45RA^-CXCR5^{hi}PD\text{-}1^{hi}$).

(B) Representative flow cytometry of Tfh cells in a cadaveric lymph node (LN control, left) and a pre-pandemic tonsil sample (tonsil control, right).

(C) Unpaired analysis of Tfh cells from HD draining LNs at V2 and V3.

(D) (left) Representative flow cytometry plots of activated $ICOS^{hi}PD\text{-}1^{hi}$ Tfh cells ($CD4^+CD8^-CD19^-CD45RA^-CXCR5^+ICOS^{hi}PD\text{-}1^{hi}$) from HD PBMCs at V1, V2, and V3. (right) Representative flow cytometry plot of CD38 expression in $ICOS^{hi}PD\text{-}1^{hi}$ Tfh cells and control CD4 T cell populations.

(E) Spearman correlation between activated $ICOS^{hi}PD\text{-}1^{hi}$ Tfh cells, defined as in (D), from PBMCs (displayed as a percentage of $CXCR5^+$ CD4 T cells) and antigen-specific GC B cells from draining LNs (displayed as a percentage of lymphocytes) of HDs at V2 (red) and V3 (blue).

In (C and E), n = 11–13. Statistical analysis: in (C), an unpaired Mann-Whitney U test with continuity correction was performed, and data are graphed as mean ± SEM. In (E), correlations were determined using the Spearman's rho with a 95% confidence interval. In (E), multivariate regression analysis (where X = Tfh cells, Y_1 = Full S^+ RBD^- GC B cells, and Y_2 = Full S^+ RBD^+ GC B cells) resulted in a Benjamini-Hochberg corrected p value of 0.85. * $p \leq 0.05$. See also Table S4.

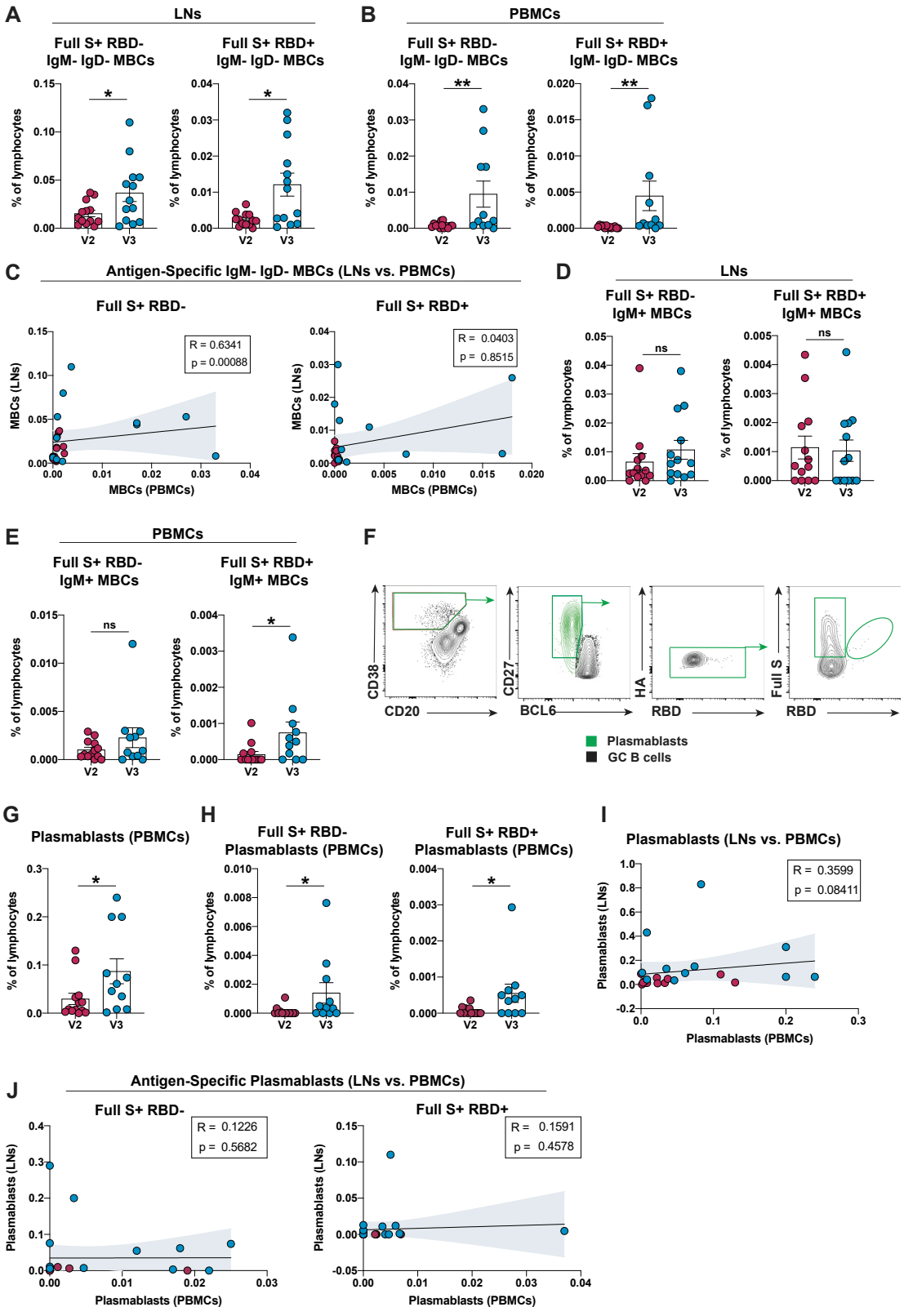

(legend on next page)

Figure S3. SARS-CoV-2 mRNA vaccines induce the generation of antigen-specific MBCs and plasmablasts, related to Figure 3

(A and B) Quantification of SARS-CoV-2-specific class-switched MBCs ($CD19^+CD4^-CD8^-IgM^-IgD^-CD38^-CD27^+$) from HD draining LNs (A) or from HD PBMCs (B) at V2 and V3.

(C) Spearman correlation between SARS-CoV-2-specific class-switched MBCs from draining LNs and PBMCs of HDs, both displayed as a percentage of lymphocytes at V2 (red) and V3 (blue).

(D and E) Quantification of SARS-CoV-2-specific IgM^+ MBCs ($CD19^+CD4^-CD8^-IgM^+CD38^-CD27^+$) from HD draining LNs (D) and HD PBMCs (E) at V2 and V3.

(F) Representative flow cytometry gating strategy of plasmablasts.

(G) Quantification of plasmablasts ($CD19^+CD4^-CD8^-IgM^-IgD^-CD38^+CD20^{lo}CD27^+BCL6^-$) in PBMCs.

(H) Quantification of (HA^-) Full S^+ RBD^- plasmablasts (left) and Full S^+ RBD^+ plasmablasts (right) in PBMCs of HDs at V2 and V3.

(I) Spearman correlation between plasmablasts from HD draining LNs and PBMCs at V2 (red) and V3 (blue), both represented as a percentage of lymphocytes.

(J) Spearman correlation between Full S^+ RBD^- plasmablasts (left) and Full S^+ RBD^+ plasmablasts (right) in LNs versus PBMCs at V2 (red) and V3 (blue).

In (A–E and G–J), n = 11–13. In (A–B, D–E, and G–H), data are graphed as mean ± SEM. Statistical analysis: in (A and B), an unpaired Mann-Whitney U test with continuity correction was performed. In (D–E and G–H), the Wald-Wolfowitz runs test was performed. In (C and I–J), correlations were determined using the Spearman's rho with a 95% confidence interval. * $p \leq 0.05$, ** $p \leq 0.01$. See also Table S4.

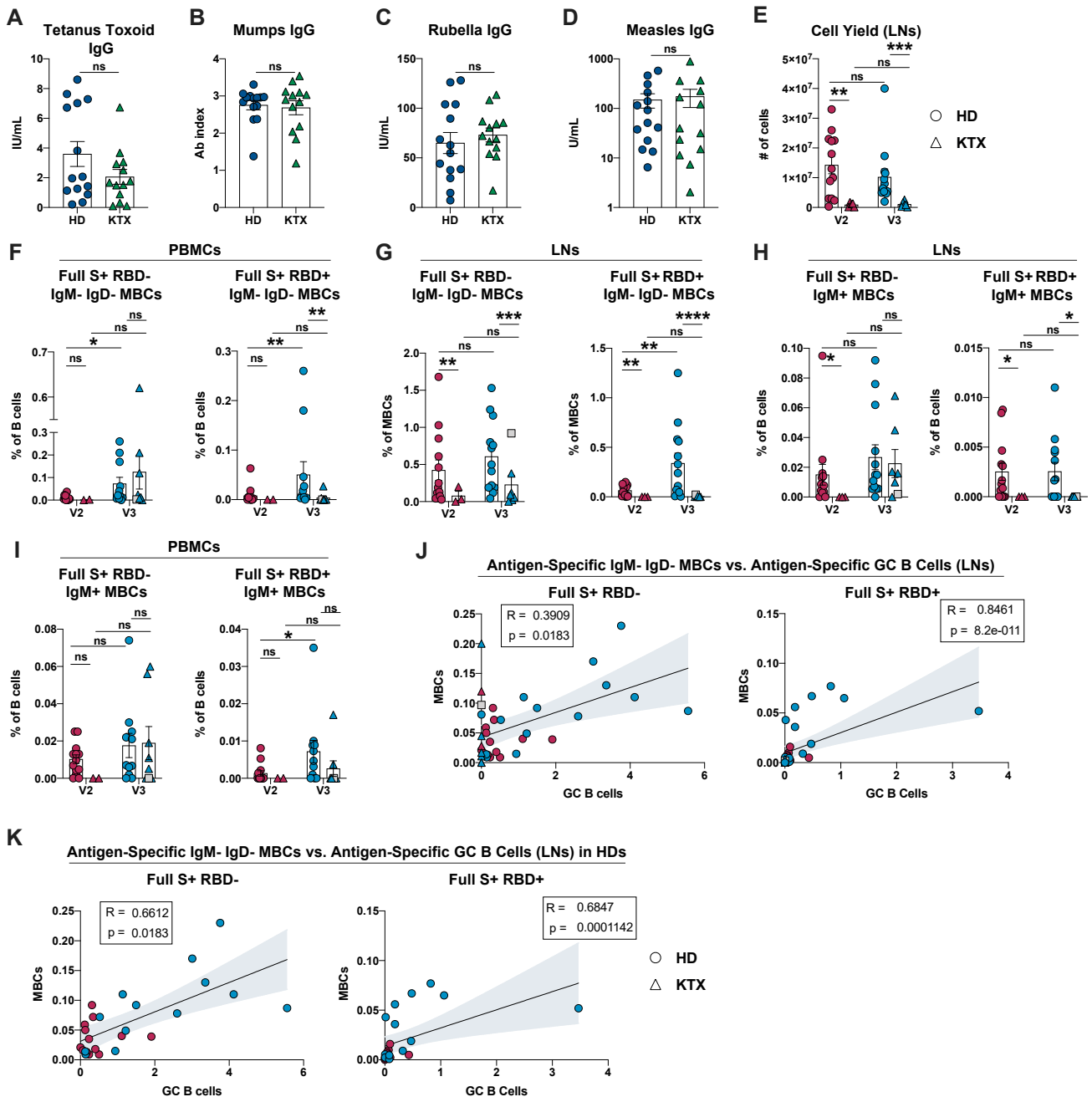

Figure S4. Kidney transplant recipients have blunted germinal centers which correlate with reduced B cell responses, related to Figure 4

(A–D) Levels of serum IgG against tetanus toxoid (A), mumps (B), rubella (C), and measles (D) in HDs and KTXs are measured by ELISA.

(E) Quantification of cell yield from draining LNs of HDs and KTXs at V2 and V3.

(F) Quantification of SARS-CoV-2-specific class-switched MBCs ($CD19^+CD4^-CD8^-IgM^-IgD^-CD38^-CD27^+$) in PBMCs from HDs and KTXs.

(G) SARS-CoV-2-specific class-switched MBCs from draining LNs of HDs and KTXs.

(H and I) Quantification of SARS-CoV-2-specific IgM^+ MBCs ($CD19^+CD4^-CD8^-IgM^+CD38^-CD27^+$) in draining LNs (H) and PBMCs (I) from HDs and KTXs.

(J and K) Spearman correlation between SARS-CoV-2-specific class-switched MBCs and SARS-CoV-2-specific GC B cells from draining LNs of HDs and KTXs (J) or from HD only (K) at V2 (red) and V3 (blue), both displayed as a percentage of B cells.

In (A–D), n = 14 for HDs and n = 13 for KTXs. In (E–K), for HDs: n = 11–13. In (E), for KTXs: n = 5 for V2 and n = 6 for V3. In (F and I), for KTXs: n = 2 for V2 and n = 8 for V3. In (G–H and J–K), for KTXs: n = 3 for V2 and n = 7 for V3. In (A–K), circles represent HDs, triangles represent KTXs, and a gray square is used to indicate a KTXs with a prior SARS-CoV-2 infection. In (E–K), red data points= V2 and blue data points = V3. In (A–I), data are graphed as mean ± SEM. Statistical analysis: in (A–E), an unpaired Mann-Whitney U test was performed. In (F–I), the Wald-Wolfowitz runs test was performed. In (J and K), correlations were determined using the Spearman's rho with a 95% confidence interval. * $p \leq 0.05$, ** $p \leq 0.01$, *** $p \leq 0.001$, **** $p \leq 0.0001$. See also Table S4.

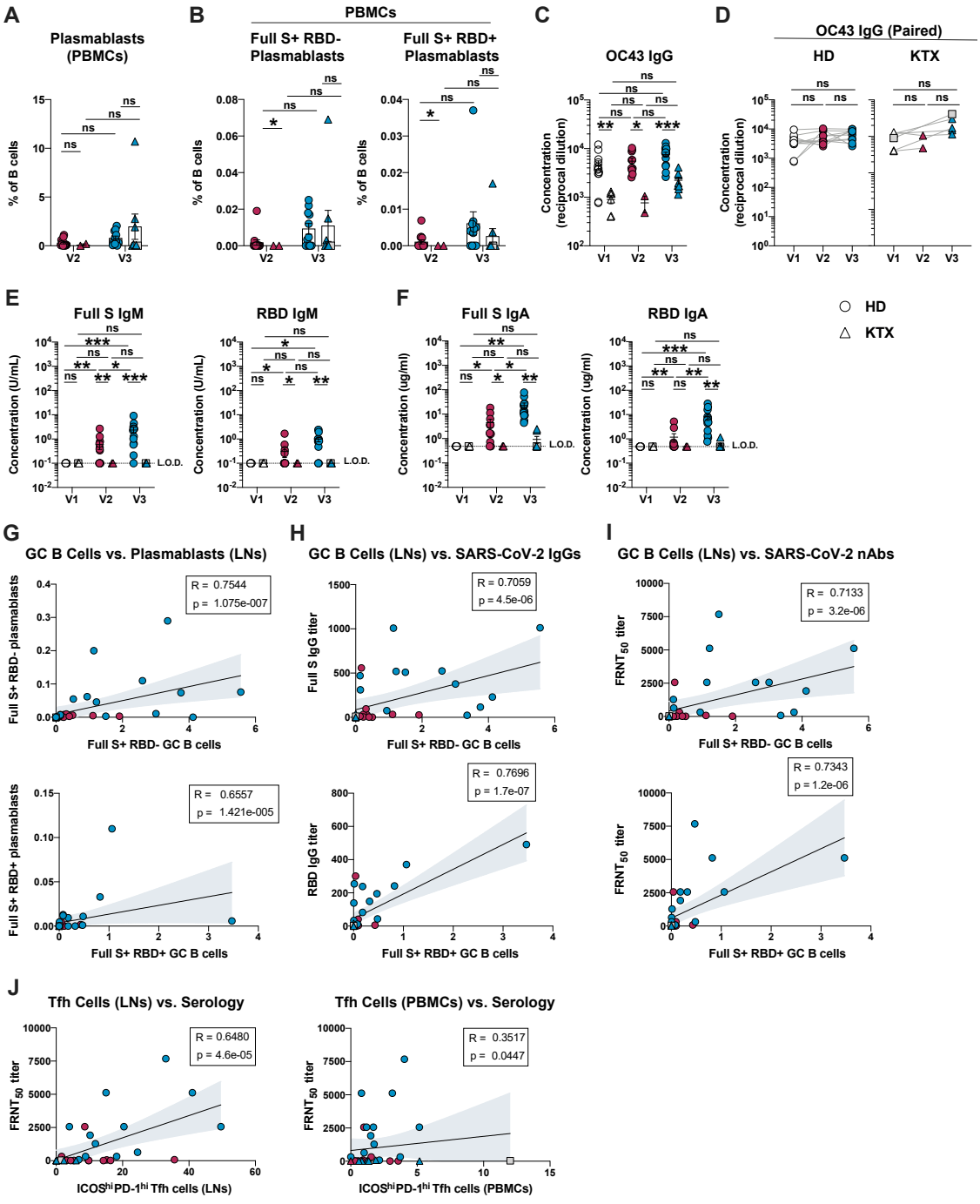

Figure S5. Kidney transplant recipients have impaired humoral responses, related to Figures 4 and 5

(A–B) Quantification of total (A) and SARS-CoV-2-specific (B) plasmablasts ($CD19^+CD4^-CD8^-IgM^-IgD^-CD38^+CD20^{lo}CD27^+BCL6^-$) in PBMCs from HDs and KTXs.

(C–D) Serum concentration of OC43-specific IgG from HDs and KTXs measured by ELISA. Data are shown as unpaired analysis (C) or as paired analysis where HDs (left) and KTXs (right) are illustrated separately (D).

(E) Serum concentration of Full S-specific (left) and RBD-specific (right) IgM from HDs and KTXs measured by ELISA.

(F) Serum concentration of Full S-specific (left) and RBD-specific (right) IgA from HDs and KTXs measured by ELISA.

(G–I) Spearman correlation between SARS-CoV-2-specific GC B cells and SARS-CoV-2-specific plasmablasts (G) and binding (H) or neutralizing antibodies (against the D614G mutant) (I) from HDs and KTXs at V2 (red) and V3 (blue). GC B cells and plasmablasts (both from draining LNs) are displayed as a percentage of B cells

(legend continued on next page)

(J) Spearman correlation between neutralizing antibody titers against the D614G mutant and activated $ICOS^{hi}PD\text{-}1^{hi}$ Tfh cells from draining LNs (left) or PBMCs (right), shown as a percentage of $CXCR5^+$ CD4 T cells, at V2 (red) and V3 (blue).

For HDs: n = 11–13; for KTXs: n = 7 for V1, n = 2 for V2, and n = 7–8 for V3. In (A–J), circles represent HDs, triangles represent KTXs, and a gray square is used to indicate a KTX with a prior SARS-CoV-2 infection. In (A–F), data are displayed mean ± SEM. Statistical analysis: in (A–F), the Wald-Wolfowitz runs test was performed. In (G–J), correlations were determined using the Spearman's rho with a 95% confidence interval. In (H), multivariate analysis (where X = Full S^+ RBD^- GC B cells, Y_1 = RBD^+ IgG, and Y_2 = S^+ IgG) resulted in a Benjamini-Hochberg corrected p value of 2×10^{-16}. In (I), multivariate analysis (where X = $FRNT_{50}$, Y_1 = Full S^+ RBD^+ GC B cells, and Y_2 = Full S^+ RBD^- GC B cells) resulted in a Benjamini-Hochberg corrected p value of 0.024.* $p \leq 0.05$, ** $p \leq 0.01$, *** $p \leq 0.001$. See also Table S4.

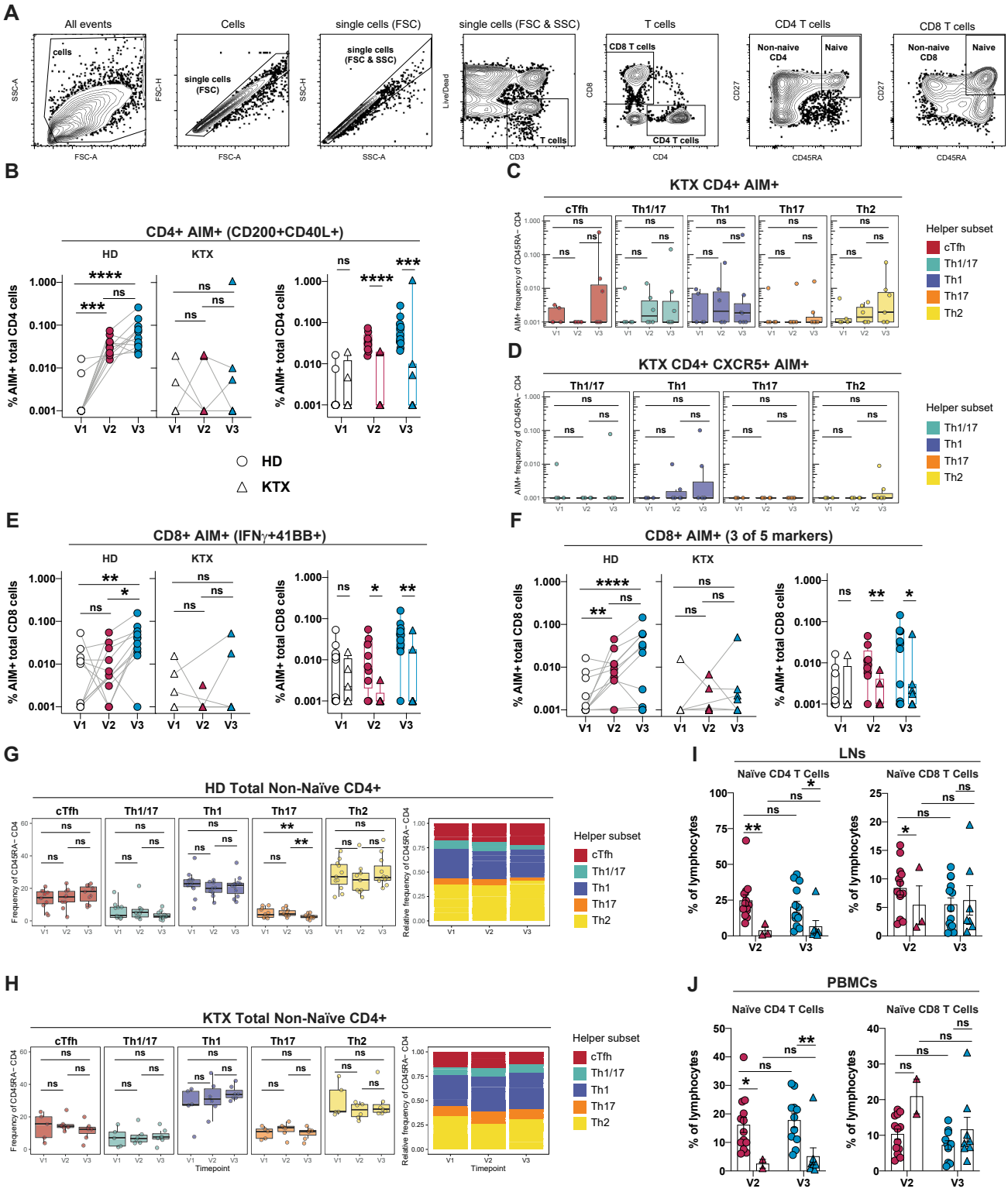

Figure S6. SARS-CoV-2-specific CD4 and CD8 T cells are reduced in KTX PBMCs, related to Figure 6

(A) Representative flow cytometry gating strategy for AIM assays on PBMC samples.

(B) Quantification of AIM$^+$ CD4 T cells as a percentage of total CD4 T cells. Paired (left) or unpaired (right) analyses of PBMC samples from HDs and KTXs at V1, V2, and V3 are shown.

(legend continued on next page)

(C and D) Quantification of AIM$^+$ CD4 T cell subsets (C) and AIM$^+$ CXCR5$^+$ CD4 T cell subsets (D) in PBMCs from KTXs.
(E and F) Quantification of AIM$^+$ CD8 T cells (IFN-γ^+ 41BB$^+$) (E) and AIM$^+$ CD8 T cells (cells expressing at least 3 of 5 activation markers: CD107a, 41BB, CD200, CD40L, and IFN-γ) (F), in PBMC samples from HDs and KTXs.
(G and H) Quantification of total CD45RA$^-$ CD4 T cell subsets in PBMC samples from HDs (G) and KTXs (H).
(I–J) Naive CD4 T cell (left) and CD8 T cell counts (right) in draining LNs (I) and PBMCs (J) from HDs and KTXs at V1, V2, and V3.
In (B–J), for HDs: n = 9–11; for KTXs: n = 5–7. In (B, E, F, I and J), circles represent HDs, triangles represent KTXs, and a gray square is used to indicate a KTX with a prior SARS-CoV-2 infection. In (B–H), boxplots represent median with interquartile range. In (I and J), data are graphed as mean ± SEM. Statistical analysis: in (B–J), the Wald-Wolfowitz runs test was used to perform an exact comparison between the two data distributions of interest. * $p \leq 0.05$, ** $p \leq 0.01$, **** $p \leq 0.0001$.